Affinity hierarchies and amphiphilic proteins underlie the co-assembly of nucleolar and heterochromatin condensates

Authors

Srivarsha Rajshekar[1], Omar Adame-Arana[2,3], Gaurav Bajpai[2,4], Serafin Colmenares[1], Kyle Lin[1], Samuel Safran[2], Gary H Karpen[1,5]

[1] Department of Molecular and Cell Biology, University of California Berkeley, Berkeley, USA

[2] Department of Chemical and Biological Physics, Weizmann Institute of Science, Rehovot, Israel

[3] Max Planck Institute for the Physics of Complex Systems, Dresden, Germany

[4] Department of Physics, Northeastern University, Boston, USA

[5] Division of Biological Sciences and the Environment, Lawrence Berkeley National Laboratory, Berkeley, USA

Correspondence: gkarpen@berkeley.edu

Abstract

Nucleoli are surrounded by Pericentromeric Heterochromatin (PCH), reflecting a close spatial association between the two largest biomolecular condensates in eukaryotic nuclei. Nucleoli are the sites of ribosome synthesis, while the repeat-rich PCH is essential for chromosome segregation, genome stability, and transcriptional silencing. How and why these two distinct condensates co-assemble is unclear. Here, using high-resolution live imaging of *Drosophila* embryogenesis, we find that *de novo* establishment of PCH around the nucleolus is highly dynamic, transitioning from the nuclear edge to surrounding the nucleolus. Eliminating the nucleolus by removing the ribosomal RNA genes (rDNA) resulted in increased PCH compaction and subsequent reorganization into a toroidal structure. In addition, in embryos lacking rDNA, some nucleolar proteins were redistributed into new bodies or 'neocondensates', including enrichment in the PCH toroidal hole. Combining these observations with physical modeling revealed that nucleolar-PCH associations can be mediated by a hierarchy of interaction strengths between PCH, nucleoli, and 'amphiphilic' protein(s) that have affinities for both nucleolar and PCH components. We validated this model by identifying a candidate amphiphile, a DEAD-Box RNA Helicase called Pitchoune, whose depletion or mutation of its PCH interaction motif disrupted PCH-nucleolar associations. Together, this study unveils a dynamic program for establishing nucleolar-PCH associations during animal development, demonstrates that nucleoli are required for normal PCH organization, and identifies Pitchoune as an amphiphilic molecular link required for PCH-nucleolar associations.

Introduction

The eukaryotic nucleus is organized into different membrane-less compartments or biomolecular condensates that assemble via phase separation or similar mechanisms driven by multivalent interactions between their constituent molecules [1,2]. An individual condensate concentrates several macromolecules, including structured and intrinsically disordered proteins and nucleic acids [3,4]. Condensates with the same components can nucleate and grow at different cellular locations and coarsen by fusions into larger clusters, whereas those with distinct compositions do not mix [5]. Nevertheless, in the crowded environment of the nucleus, different condensates display close, conserved associations to form higher-order complex structures [6]. Although many studies have examined the formation and function of individual condensates, how distinct interacting condensates form and impact each other *in vivo* is less clear. This study addresses this question in the context of the two largest nuclear condensates, the nucleolus and heterochromatin.

The nucleolus is the site of ribosome synthesis with additional functions in cell cycle progression, stress response, and protein sequestration [7]. The nucleolus assembles on chromosomal loci with transcribing ribosomal RNA genes (rDNA) and recruits specific factors involved in ribosomal RNA (rRNA) transcription, processing, and ribosome assembly to form three sub-compartments with different compositions and material properties [8,9]. This organization is thought to facilitate the vectorial expulsion of ribosomes through and out of the nucleolus [10,11]. In most eukaryotic nuclei, the nucleolus is surrounded by Pericentromeric Heterochromatin (PCH), a chromatin compartment composed of megabases of pericentromeric repeats, including tandemly repeated satellite DNA and transposable elements[12,13]. PCH is associated with transcriptional silencing and has essential roles in nuclear architecture, chromosome segregation, and genome stability [14]. Under the microscope, PCH can be visualized as chromatin regions enriched for the AT-rich DNA dye DAPI, histone modifications di- and tri-methylation of histone H3 (H3K9me2/3), and the cognate epigenetic reader Heterochromatin Protein 1 (HP1) [15]. HP1 is a multivalent protein with structured and disordered domains [16] that phase separates and partitions DNA and nucleosomes *in vitro* [17,18], and forms a liquid-like condensate nucleated by H3K9me2/3 enriched chromatin *in vivo* [19–21]. One explanation for why the nucleolus is adjacent to PCH is that tandem repeats of rDNA are positioned next to heterochromatic satellite repeats on a subset of chromosomes [22]. However, cytological and sequencing analyses have revealed that sequences from most chromosomes (including those lacking rDNA) make contacts with the nucleolus [23–25], suggesting that cis-proximity to rDNA is not necessary for PCH to organize at the nucleolar edge. The mechanisms that position PCH from all chromosomes around the nucleolus are unclear. Understanding this is important, as PCH dissociation from nucleoli

in senescent cells suggests a link between PCH-nucleolar association and cellular health [26].

In this study, we use live imaging and genetic tools in the *Drosophila melanogaster* model to uncover the dynamic patterns of *de novo* assembly of PCH from all chromosomes around the nucleolus. Removal of rDNA, and thus a functional nucleolus, caused dramatic changes in PCH assembly dynamics and redistribution of some nucleolar proteins into new bodies or 'neocondensates'. These *in vivo* phenotypes led us to develop a physical model based on a hierarchy of interaction strengths between PCH, nucleoli, and 'amphiphilic' protein(s) able to interact with both nucleolar and PCH components. Simulations recapitulated the layered organization of nucleoli and PCH, as well as the phenotypes caused by rDNA deletion. Importantly, this model was validated by demonstrating that Pitchoune, a DEAD-box RNA-Helicase protein, acts as an amphiphilic linker responsible for PCH-nucleolar associations. We propose that disrupting affinity hierarchies between interacting condensates can redistribute their constituents to form neocondensates or other aberrant structures that may result in cellular disease phenotypes.

Results

Dynamic conformational changes during assembly of PCH around the nucleolus during *Drosophila* embryonic development

As in other eukaryotes, *Drosophila* nucleoli are multi-layered [9,27], with the outermost layer Granular Component (GC) marked by Modulo (the fly ortholog of Nucleolin) and the Dense Fibrillar Component (DFC) marked by Fibrillarin. Live imaging in late embryos (~12-16 hr, Embryonic Stage 14-16) co-expressing fluorescently tagged transgenes of Fibrillarin or Modulo along with HP1a, shows that HP1a is positioned around the GC at the apical edge of the nucleus (**Fig. 1a, Extended Data Fig. 1a).** In the canonical 'surrounded' conformation, HP1a does not fully engulf the nucleolus but organizes around its lateral sides, covering ~30% of the nucleolar surface in 3D (**Supplementary Movie 1**). This surrounded conformation persists through development, as observed in gut cells in late embryos, epidermal cells in first instar larvae, and eye discs in third instar larvae (**Extended Data Fig. 1b)**.

To determine how PCH forms the surrounded conformation around the nucleolus, we performed high-resolution time-lapse imaging of HP1a and Fibrillarin in early *Drosophila* embryos. *Drosophila* embryos undergo 14 syncytial nuclear divisions before cellularization at the blastoderm stage, with chromatin features such as H3K9 methylation progressively established during these cycles [28]. PCH condensates first emerge in cycle 11 [19] while nucleoli first emerge in cycle 13 [29], making cycle 13 the earliest time both condensates appear in the same nucleus. Upon entry into cycle 13 interphase, HP1a and Fibrillarin proteins are initially diffuse throughout the nucleus, then within ~8 mins, each

113 becomes enriched in multiple, distinct foci (**Fig. 1b(i) and Supplementary Movie 2**).
114 Small PCH and nucleolar condensates remain separated throughout cycle 13, likely
115 because growth is limited by the short interphase (~15 mins) before both dissolve in
116 mitosis [19,29]. Cycle 14 begins like cycle 13 in that HP1a and Fibrillarin foci emerge soon
117 after mitotic exit and are initially separated. During the longer interphase (90 min) of cycle
118 14, PCH and nucleoli undergo extensive growth in volume and self-fusions [19,21,29].
119 However, instead of forming the canonical surrounded conformation, PCH extends away
120 from the nucleolus while being tethered to the nucleolus at one end, hereafter referred to
121 as the 'extended conformation' (**Fig. 1b(ii) and Supplementary Movie 3**). The extended
122 conformation is also observed in nuclei with two nucleoli, which appear when the two
123 rDNA arrays in a nucleus are unpaired (**Extended Data Fig. 1c**).

124 Continued live imaging of HP1a and Fibrillarin in post-blastoderm, asynchronous cell
125 divisions revealed how the extended PCH configuration dynamically transitions into the
126 surrounded form observed in later developmental stages. PCH rapidly forms the extended
127 configuration by lining the nuclear edge through the rest of cycle 15 (**Fig. 1b(iii) and**
128 **Supplementary Movie 4**), transitions between the extended and surrounded
129 configurations during cycle 16 (**Fig. 1b(iv) and Supplementary Movie 5**) and stably
130 wraps around the nucleolus ~15 min into cycle 17 interphase (**Fig. 1b(v) and**
131 **Supplementary Movie 6**). HP1a occupancy around the nucleolus increases from 10%
132 to 30% in 3D between cycles 14 and 17 (**Fig. 1c**). HP1a reorganization observed in Cycle
133 17 is mirrored in cultured S2 cells exiting mitosis, where HP1a transitions through an
134 'extended' intermediate before stably surrounding the nucleolus (**Extended Data Fig. 1d**).

135 Next, we performed DNA FISH for pericentromeric repeats and rDNA to determine how
136 PCH and nucleolar DNA sequences are reorganized in 3D during development. In the
137 early embryo, PCH is connected to the nucleolus due to the physical proximity of rDNA
138 repeats to pericentromeric repeats on the X and Y chromosomes in both females (XX)
139 and males (XY) (**Extended Data Fig. 2a-b**). In the late embryo, we observed an intense
140 rDNA signal at the nucleolar periphery, adjacent to the 359bp sequence on the X
141 chromosome (**Extended Data Fig. 2c**). This is consistent with the process of nucleolar
142 dominance, where the rDNA array on one X chromosome is silenced in *Drosophila*
143 *melanogaster* [30,31], and with the repositioning of silent rDNA outside the nucleolus [32]. The
144 1.686 repeat sequences, located on chromosomes lacking rDNA (chromosomes 2 and
145 3), are positioned away from the nucleolus during cycle 15 (Stage 8), forming the
146 'extended conformation', but relocate to the nucleolar edge in the late embryo (**Extended**
147 **Data Fig. 2d-e**). Immunostaining early embryos for H3K9me2/3, Lamin, and Fibrillarin
148 reveals that the PCH lines the nuclear lamina in the 'extended conformation' (**Fig. 1d**).

149 Together, these experiments detail the reorganization of the two largest biomolecular
150 condensates during *Drosophila* embryonic development at high spatial and temporal
151 resolution. We observe that PCH and nucleolar condensates undergo independent

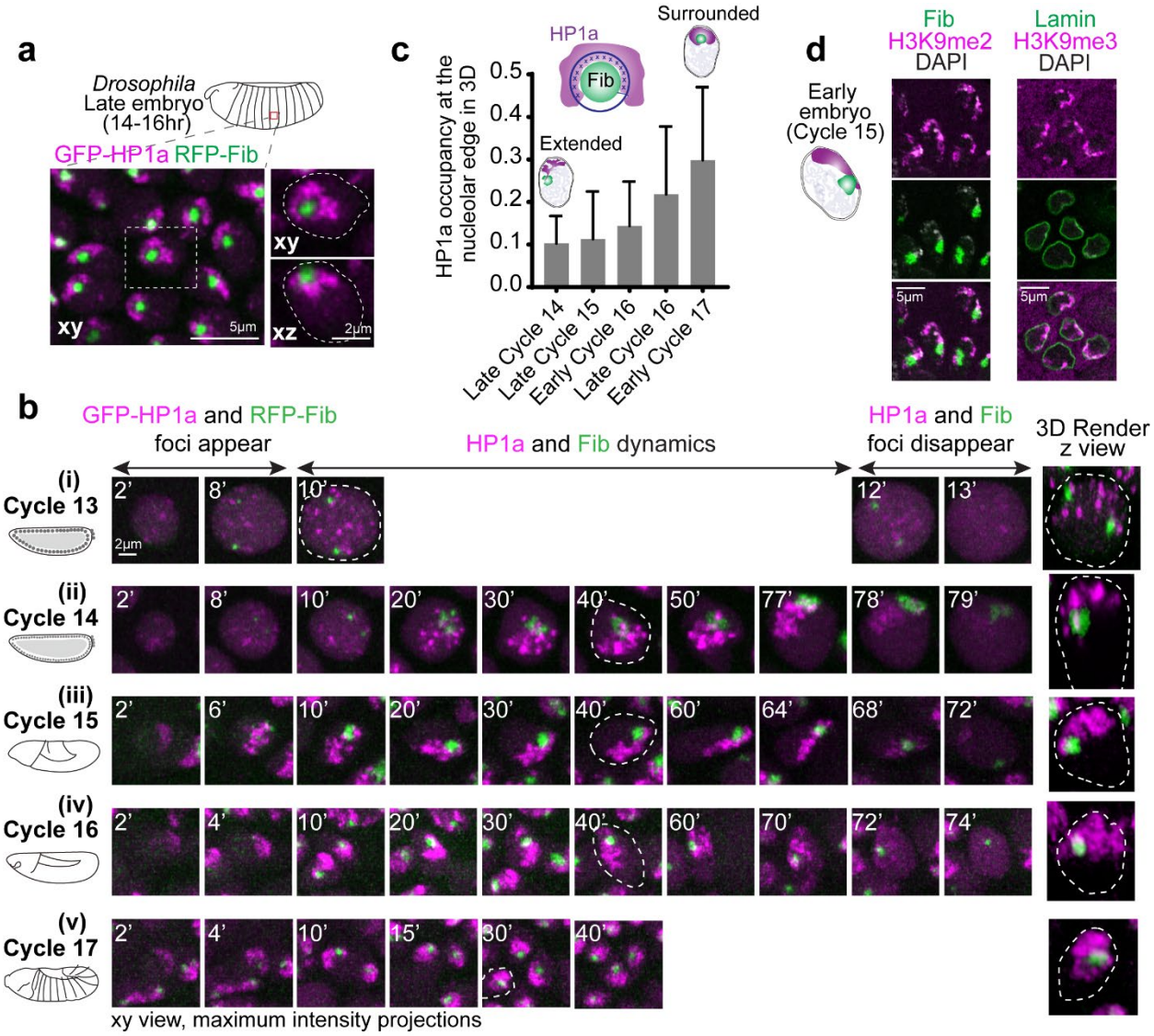

Fig. 1: PCH is reorganized during *Drosophila* embryonic development from extended away to positioned around the nucleolus. (**a**) Maximum intensity projections showing the distribution of GFP-HP1a (magenta) and RFP-Fibrillarin (green) in live epidermal nuclei from a late-stage *Drosophila* embryo (Stage 16, ~14-16hr). The nucleus outlined by the white dashed box is magnified on the right, presenting xy and xz views with white dashed lines indicating the nuclear boundary. (**b**) Maximum intensity projections (xy view) of individual live nuclei of GFP-HP1a (magenta) and RFP-Fibrillarin (green) localization in Cycles 13-17 of *Drosophila* embryogenesis. The numbers on the top left corner of each image indicate time (in minutes) after mitotic exit. The 3D render of the nucleus marked with white dashed lines is presented (not to scale) at the right end of the panel. (**c**) Quantification of HP1a occupancy at the nucleolar edge during specific developmental cycles. "Early Cycle" refers to nuclei between 15-30 mins into the specified interphase, "Late Cycle" refers to nuclei between 50-70 mins. Schematic above the graph illustrates the approach used to calculate the fraction of the nucleolar edge (dark blue shell) intersecting with HP1a (dark blue crosses). Bar graphs represent mean with s.d. n>50 nuclei (from 5 embryos) at each time point. (**d**) Immunofluorescence staining of nuclei from early (Cycle 15) embryos. Left: H3K9me2 (magenta) and Fibrillarin (green). Right: H3K9me3 (magenta) and Lamin (green).

152 nucleation, growth, and fusion, displaying cycle-specific differences while dynamically
153 transitioning from the extended (predominantly nuclear periphery associated) to the
154 surrounded configurations (nucleoli associated) (summarized in **Extended Data Fig. 2f**).

155 **Embryos lacking nucleoli display increased PCH compaction and neocondensate**
156 **formation**

157 The specific patterns of PCH reorganization around the nucleolus during embryonic
158 development prompted us to ask if the nucleolus impacts PCH assembly dynamics. We
159 imaged RFP-HP1a and GFP-Fib in embryos that lack any rDNA repeats (designated
160 hereafter as -rDNA) due to a rearranged X chromosome (C(1)DX/0). No functional
161 nucleoli are formed in -rDNA embryos [29], but they develop through early embryogenesis
162 due to maternal deposition of ribosomes. Fibrillarin forms spherical structures (as
163 previously reported by Falahati et al. 2016 [29]), which are located at a significantly longer
164 distance from the HP1a/PCH condensate compared to their distance in wildtype (+rDNA)
165 controls (**Fig. 2a-b;** +rDNA mean=1.78μm, -rDNA mean=3.69μm, $p<0.0001$). This result
166 suggests that Fibrillarin and HP1a proteins do not interact directly. Instead, when factors
167 responsible for nucleolus formation (rDNA/rRNA) are not present, Fibrillarin self-
168 associations [33] and/or secondary affinities with other structures or molecules are sufficient
169 to cause the formation of new enrichments (hereafter termed 'neocondensates') not found
170 in wildtype cells. The 'extended' HP1a conformation typically observed in cycles 14 and
171 15 is replaced by a collapsed, rounded structure at the apical end of -rDNA nuclei (**Fig.**
172 **2a, c**). The aspect ratio (major axis/minor axis) of the HP1a domain is significantly
173 reduced (**Fig. 2d**; +rDNA mean=1.96, -rDNA mean=1.40, $p<0.0001$). Additionally, the
174 distance between pericentromeric repeats 1.686 (on Chr 2 and 3) and AAGAG (satellite
175 repeats on all chromosomes) is decreased in -rDNA nuclei compared to +rDNA controls
176 (**Fig. 2e-f**; +rDNA mean=0.74μm, -rDNA mean=0.32μm, $p<0.0001$). Thus, PCH loses the
177 extended configuration and shows increased compaction in the absence of
178 rDNA/nucleoli, where compaction is defined by the reduction in 3D space between PCH
179 elements.

180 To our surprise, PCH transitioned to a toroidal (donut-like) structure in all imaged cells in
181 late-stage -rDNA *Drosophila* embryos, with a core devoid of HP1a ('PCH void') (**Fig. 3a**).
182 We visualized this transition at increased spatial resolution in the large nuclei of the
183 amnioserosa, which forms a monolayer on the dorsal surface of the embryo during
184 gastrulation [34] (**Fig. 3b-c and Supplementary Movie 7**). In addition to the absence of
185 HP1a, the PCH void also lacked the major nucleolar proteins Fibrillarin (**Fig. 3c**), which
186 formed a separate neocondensate, and Modulo, which dispersed in the nuclear space
187 (**Extended Data Fig. 3a**). The PCH void did not contain DNA (DAPI staining), histones
188 marked with H3K9me2 (IF) (**Extended Data Fig. 3c**), or any significant accumulation of
189 RNAs (Propidium Iodide staining) (**Extended Data Fig. 3d**). However, treatment with 488

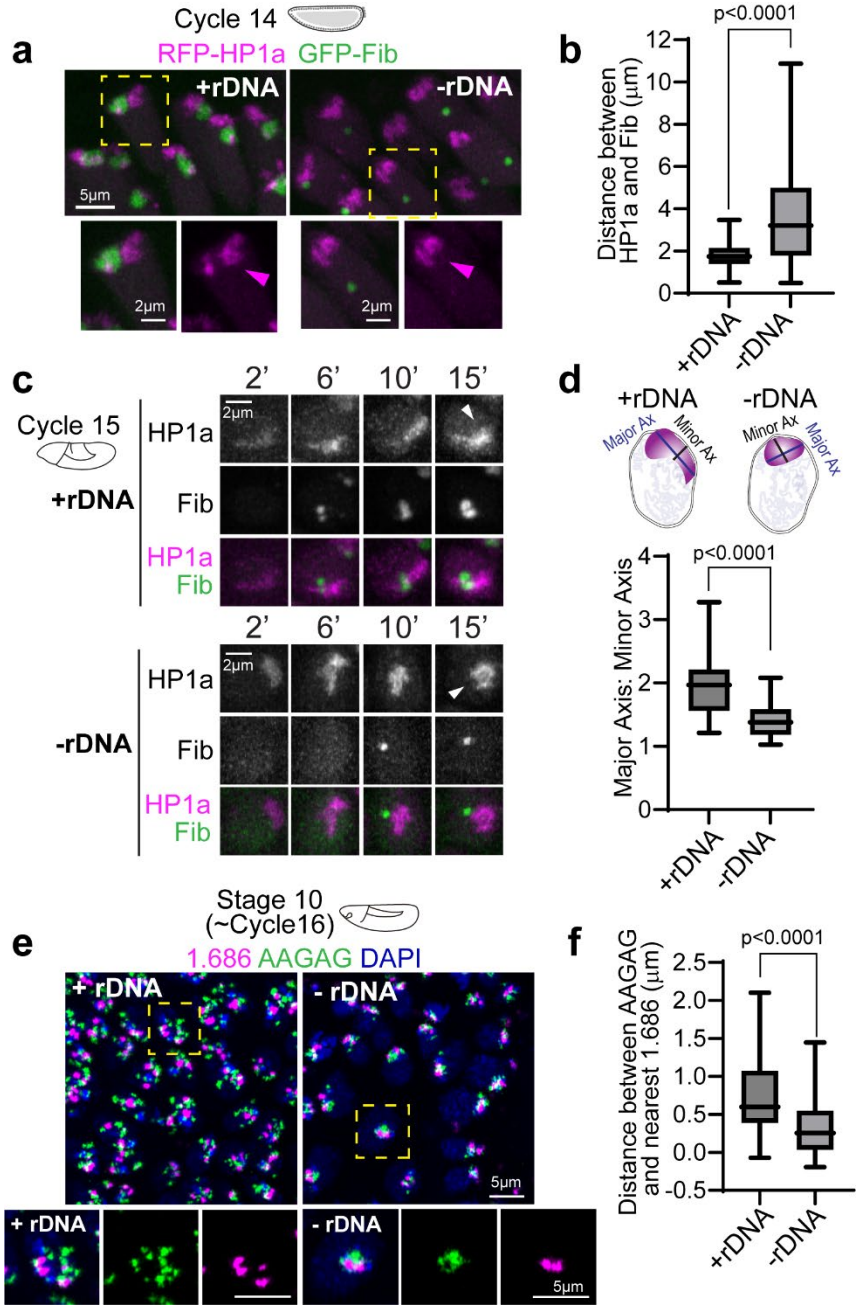

Fig. 2: Increased PCH compaction in embryos lacking rDNA. (**a**) Maximum intensity projections of live nuclei from wildtype embryos (+rDNA) and mutant embryos lacking rDNA (-rDNA) at Cycle 14, expressing RFP-HP1a (magenta) and GFP-Fibrillarin (green). The dashed yellow box highlights the nucleus enlarged in the panel below. (**b**) Distance between the centers of geometry of HP1a and Fibrillarin in +rDNA and -rDNA embryos. n>200 nuclei (from 5 embryos) for each genotype. (**c**) Maximum intensity projections from live imaging of nuclei from +rDNA and -rDNA embryos showing the reassembly of RFP-HP1a (magenta) and GFP-Fibrillarin (green) at the indicated minutes after the start of Cycle 15. White arrowheads point to HP1a organization 15 minutes after the start of Cycle 15 in +rDNA and -rDNA embryos. (**d**) Quantification of the aspect ratio (major axis over minor axis) of HP1a segments 15 minutes after the start of Cycle 15 in +rDNA and -rDNA embryos. n>30 nuclei in each genotype. (**e**) Maximum intensity projections of FISH (Fluorescence in Situ Hybridization) of satellite repeats 1.686 (magenta) and AAGAG (green) in DAPI (blue)-stained nuclei in +rDNA and -rDNA Stage 10 embryos. The dashed boxes mark the nuclei enlarged on the right. (**f**) Quantification of the distance between AAGAG and its nearest 1.686 locus. n>40 pairs of loci in each genotype. Box plots extend from 25th to 75th percentile. Error bars: Min to Max.

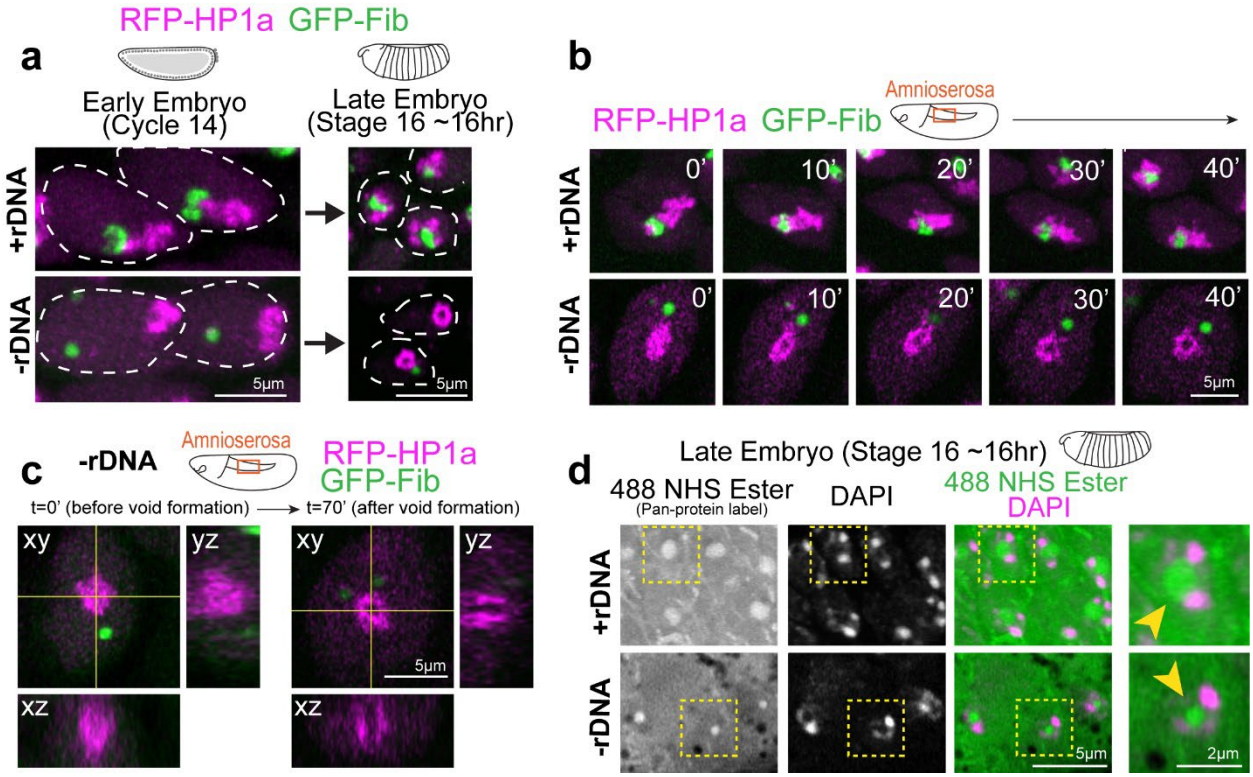

Fig. 3: A protein-filled core reshapes the PCH condensate to a toroid-like structure in -rDNA developing embryos. (**a**) Representative stills of live +rDNA and -rDNA nuclei at Cycle 14 and in Stage 16 (late stage) embryos showing RFP-HP1a (magenta) and GFP-Fibrillarin (green). (**b**) Time-lapse stills (single slices) of a +rDNA and -rDNA amnioserosa nucleus with HP1a (magenta) and Fibrillarin (green). T=0 mins was set to capture the time window where PCH transitions from a compacted to a toroidal structure in -rDNA amnioserosa nuclei. (**c**) Orthogonal projections along yellow intersecting lines in an amnioserosa nucleus from a -rDNA embryo before and after the formation of the 'PCH void'. (**d**) Late embryos (Stage 16) with the +rDNA or -rDNA genotype co-stained with a pan-protein label, 488 NHS Ester (green), and DAPI (magenta) show that the 'PCH void' in -rDNA embryos is enriched for proteins (yellow arrowhead). Nuclei marked with the yellow dashed box are enlarged on the right.

NHS Ester, a pan-protein label [35], revealed that the PCH void was enriched for proteins (**Fig. 3d**).

We conclude that PCH initially displays an atypical, compacted morphology in embryos lacking rDNA and nucleoli. As development proceeds, the PCH morphs into an abnormal toroidal structure whose central core (the PCH void) lacks HP1a, nucleolar proteins, chromatin, and RNA but is filled with protein(s) that may represent another neocondensate. Together, these results reveal that nucleoli are required to organize PCH in the 3D nuclear space by preventing PCH hyper-compaction and that disrupting interactions within or between condensates can create new nuclear structures.

Coarse-grained modeling recapitulates *in vivo* PCH-nucleolar organization phenotypes and highlights a potential role for amphiphilic proteins in mediating their association

Since the nucleolus and PCH assemble via phase separation or similar mechanisms [8,19,21,36], we drew inspiration from the physical theory of three-phase wetting to better understand PCH-nucleolar organization in the nucleoplasm. This theory states that an equilibrium between the interfacial tensions (i.e., the energetic cost of forming an interface between two phases) determines the spatial configurations of the different phases [37] (**Fig. 4a**, fully engulfing, partial engulfing, or individual separated phases). These interfacial tensions are dictated by the relative interaction strengths between the components of the different phases. To describe the different three-phase spatial configurations we introduced the spreading coefficient of a phase i, S_i,

$$S_i = \gamma_{jk} - (\gamma_{ij} + \gamma_{ik})$$

where the letters $i, j,$ and k, represent three different phases, γ_{jk} is the interfacial tension between phases j and k, γ_{ij} is the interfacial tension between phases i and j, and γ_{ik} is the interfacial tension between phases i and k. For every three-phase combination, there are three spreading coefficients, and depending on whether such spreading coefficients are positive or negative, different spatial configurations are attained [37]. We exemplify this using PCH (H), the outermost nucleolar layer GC (G), and the nucleoplasm (N) (**Fig. 4a**).

To connect the theory of wetting with our *in vivo* results, we used a minimal coarse-grained model that incorporates the molecular interactions and biophysical parameters that could mediate nucleolar-PCH spatial organization with four minimal components (**Fig. 4b**). (i) PCH (H) as a long, self-attracting polymer. (ii) Fibrillarin (F), which represents a self-associating nucleolar protein. (iii) rDNA (rD) as a polymeric block within the chromatin fiber that experiences good solvent conditions and is flanked by two PCH blocks. Although we do not explicitly account for the presence of rRNA, we use rDNA as a proxy for the nucleating site for Fibrillarin condensates. Finally, (iv) Protein (X), as a self-associating molecule with an affinity for PCH. These properties were attributed to protein X to account

227 for the spherical protein-rich compartment that consistently formed within the PCH-void
228 in -rDNA nuclei (**Fig. 3d**). We then considered what additional properties Protein X could
229 possess to form the observed *in vivo* organization of the nucleolus and PCH.

230 To recapitulate the layered PCH-nucleolar organization, we reasoned the self-
231 associations of Fibrillarin must be stronger than those of protein X, which in turn must be
232 stronger than the self-interactions of PCH. These self-interaction choices result in the
233 following hierarchy of interfacial tensions $\gamma_{FN} > \gamma_{XN} > \gamma_{HN}$, where γ_{iN} is the interfacial
234 tension between a phase enriched in component $i = F, X,\ H$ and the nucleoplasm (N).
235 Additionally, we note that for a stable association between PCH and the Fibrillarin-rich
236 phase, Protein X must also have an affinity for Fibrillarin (or more generally for nucleolar
237 components), which *in vivo* might be mediated by the presence of rRNA. Therefore, we
238 define Protein X as an 'amphiphilic protein', due to its dual affinity for the PCH and
239 nucleolar phases, as defined previously for synthetic co-condensates [38]. Altogether, these
240 considerations led us to define a hierarchy of interaction strengths (rD-F ≥ F-F > X-X > F-
241 X > X-H > H-H) as an initial set of parameters listed in the 4x4 interaction matrix (**Fig. 4c**).
242 Simulating this affinity hierarchy recapitulated the canonical PCH-nucleolar organization
243 observed in +rDNA animals *in vivo* (**Fig. 4c and Supplementary Movie 8**). Various
244 scenarios incompatible with the experimental observations of the layered organization of
245 the nucleolus and PCH arise by deviating from the hierarchy of self-interaction strengths
246 in the simulations. For example, instead of having a complete engulfing of the nucleolus
247 by PCH, there are partial engulfing or no engulfing scenarios when the interaction
248 between the amphiphilic proteins is larger than that of Fibrillarin (**Extended Data Fig. 4d**).
249 Importantly, our choice of interaction parameters is not unique as long as the interfacial
250 tensions fulfill $\gamma_{FN} > \gamma_{XN} > \gamma_{HN}$, we obtain a complete engulfing of the nucleolus by PCH.
251 A detailed rationale for the choice of parameters is described in the Methods section.

252 Next, we modeled the consequences of removing rDNA by setting the rDNA-Fibrillarin
253 interactions to zero, thus eliminating its ability to recruit nucleolar components such as
254 Fibrillarin and X. Reducing the attraction between Fibrillarin and the amphiphilic protein
255 X, which increases the interfacial tension between the Fibrillarin-rich and the amphiphilic-
256 rich phases, γ_{FX}, resulted in the formation of a protein X neocondensate within the PCH
257 void and a spatially separated Fibrillarin neocondensate (**Fig. 4d-e**), as observed in
258 -rDNA embryos *in vivo* (Fig. 2 and 3). These phenotypes are observed in simulations
259 whenever the protein X – PCH interaction strength is greater than or equal to the X –
260 Fibrillarin interactions (i.e., X-H ≥ F-X) (**Extended Data Fig. 4e-f**). In the model, the
261 nucleation of the new phase of amphiphilic protein X occurs within the PCH to reduce the
262 cost of creating an interface of protein X with the solvent. Instead, being surrounded by
263 PCH can reduce this interfacial energy, as expected from a wetting picture of simple
264 liquids [37]. We conclude that incorporating affinity hierarchies and an amphiphilic protein
265 X into a minimal model recapitulates the observed *in vivo* organization of PCH and

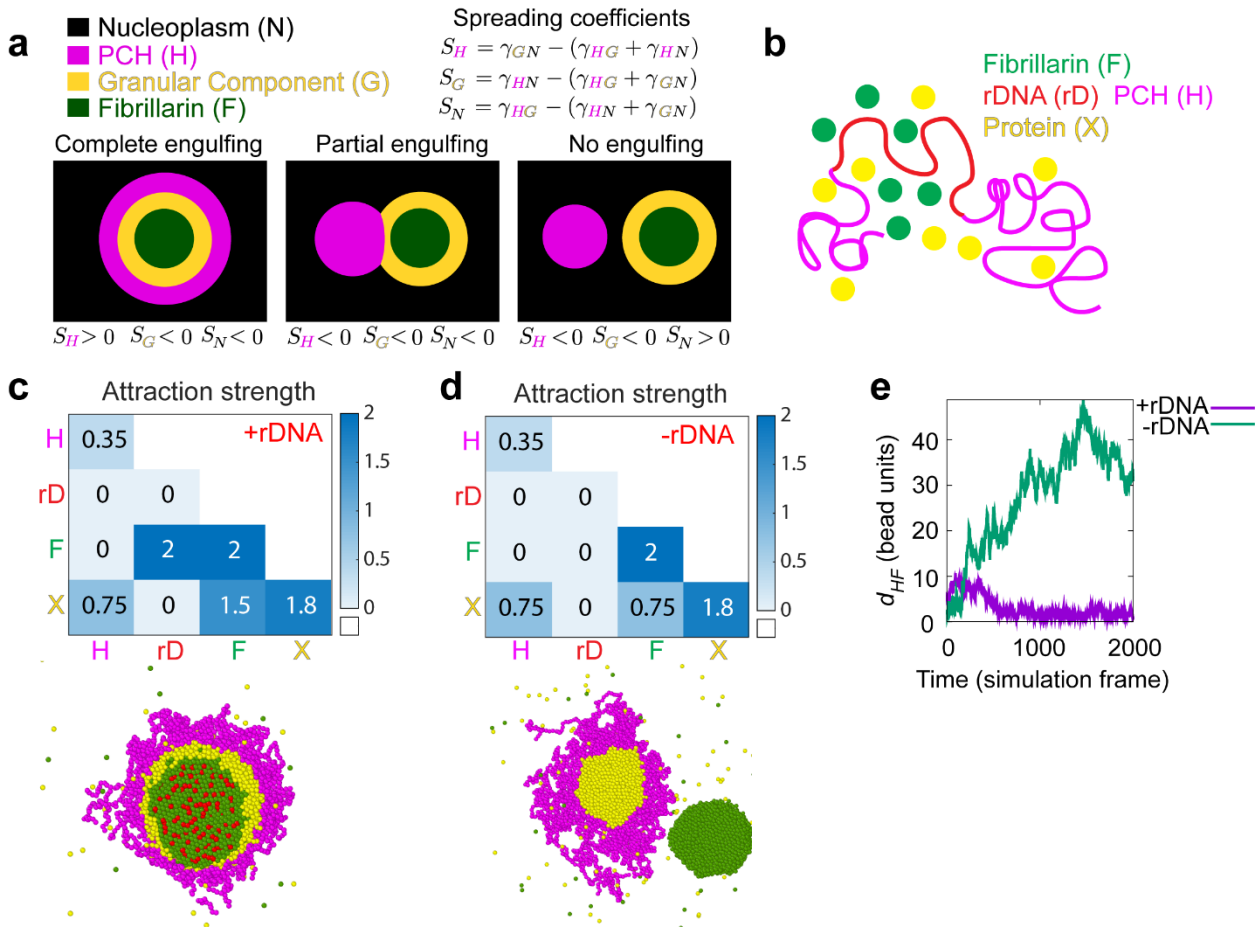

Fig. 4: A hierarchy of interaction strengths between PCH, nucleoli and 'amphiphilic' protein(s) recapitulates their +rDNA and -rDNA *in vivo* organization. (**a**) The schematic shows the spatial organization of three different phases. The interfacial tensions, γ_{ij}, between phases *i* and *j* (where *i* and *j* can be nucleoplasm (N) in black, PCH (H) in magenta, or the granular component (G) in yellow) are used to define the spreading coefficients, *Si*, shown in the top right corner. Given the assumption that $\gamma_{GN}>\gamma_{HN}$, the three possible combinations of spreading coefficients determine the configuration of the three phases, ranging from complete engulfing to partial engulfing to no engulfing. Since the Fibrillarin-rich phase (F) is always within a functional nucleolus, its spreading coefficients are not included in this analysis. (**b**) Course-grained modelling of nucleolar-PCH assembly with four minimal components: PCH (H) as a self-interacting polymer (magenta) rDNA (rD) as polymeric block embedded within PCH (red), Fibrillarin (F) as a representative of a self-associating nucleolar protein (green), and a self-associating protein 'X' (yellow) representing those enriched in the PCH void in -rDNA nuclei. (**c** and **d**) The matrices indicate the strengths of interaction (blue gradient, units: k_BT) between Fibrillarin (F) (green), rDNA (rD) (red), PCH (H) (magenta), and protein (X) (yellow), which has dual affinities for both H and F. The indicated affinity hierarchies result in simulated outcomes that recapitulate their +rDNA and -rDNA organization observed *in vivo*. (**e**) Distance (d_{HF}) between the centers of mass of PCH (H) and Fibrillarin (F) clusters in +rDNA and -rDNA simulations.

nucleolar condensates in both +rDNA and -rDNA conditions. This led us to predict that in WT conditions, protein X would be a self-associating protein with dual affinities for the nucleolus and PCH, albeit with a weaker affinity for PCH components (F-X > X-H).

The DEAD-box RNA Helicase Pitchoune is a granular compartment protein that forms a neocondensate within PCH in -rDNA embryos

A candidate for an amphiphilic protein that can interact with both PCH and the nucleolus emerged from Falahati et al., 2017 [36]. They reported that the DEAD-box RNA helicase Pitchoune (Pit), typically a granular component (GC) nucleolar protein [39], mislocalized to the apical part of the nucleus in cycle 14 -rDNA embryos, similar to the compacted PCH domain observed in our studies (Fig. 2a). Pitchoune, the *Drosophila* ortholog of DDX18, is required for larval development [39], and possesses an N-terminal intrinsically disordered region (IDR), a central helicase core, and a disordered C-terminal domain (**Fig. 5a**). We identified two tandem "PxVxL" HP1a-interacting motifs [40,41] in the C-terminal tail of Pitchoune with PVVDL being conserved across eukaryotes along with LKVGA being conserved among Drosophilids (**Fig. 5a and Extended Data Fig. 5a**). Additionally, Pitchoune belongs to the DDX family of proteins, other members of which phase separate and modulate condensate behavior [42]. Together, these clues led us to hypothesize that Pitchoune could be a candidate amphiphilic protein that can 1) form condensates and 2) have a dual affinity for both the nucleolus and PCH.

Consistent with its role as a GC nucleolar protein [43], Pitchoune is enriched in the outermost nucleolar compartment in *Drosophila* embryos and S2R+ cells (**Fig. 5a**). Next, to investigate whether Pitchoune is enriched in the PCH void in -rDNA embryos, we performed live imaging in +rDNA and -rDNA embryos co-expressing Pit-GFP and RFP-HP1a transgenes. In cycle 14 +rDNA nuclei, Pitchoune localizes to the nucleolus while HP1a is in the extended configuration. In contrast, a faint Pitchoune signal co-localizes with the more compact HP1a domain in -rDNA nuclei (**Fig. 5b**). In cycle 17 epidermal nuclei and amnioserosa nuclei, HP1a surrounds Pitchoune in +rDNA embryos, whereas in -rDNA embryos, high-intensity Pitchoune puncta appear within each compacted HP1a condensate (**Fig. 5b**). Time-lapse imaging of amnioserosa nuclei in -rDNA embryos revealed that Pitchoune is initially faintly mixed but gradually separates from HP1a, with the intensity of Pitchoune increasing ~2.5-fold over an hour (**Fig. 5c-d and Supplementary Movie 9**). Furthermore, the circularity of Pitchoune increases and approaches 1 (in projections) (**Fig. 5e**), and the area of Pitchoune decreases over time (**Fig. 5f**). These results suggest that Pitchoune demixes from HP1a and forms a spherical neo-condensate surrounded by PCH, minimizing interfacial energy by avoiding the creation of a larger energy interface between Pitchoune and the nucleoplasm (**Fig. 5g**).

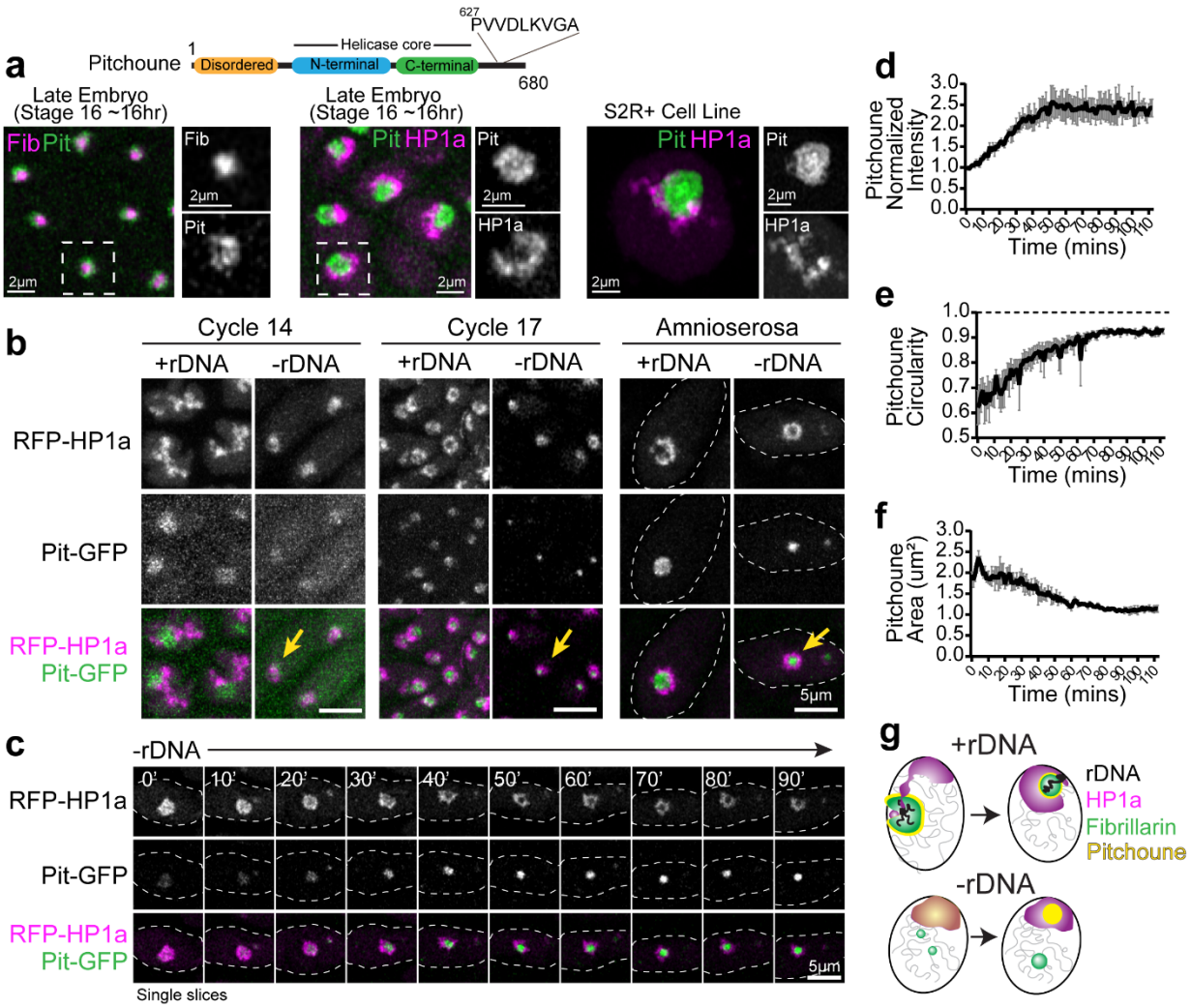

Fig. 5: The RNA Helicase Pitchoune is enriched in the PCH void in -rDNA embryos. (**a**) Protein Subdomains in Pitchoune (Pit) with an N-terminus disordered domain, central helicase core and C-terminus with a conserved HP1a interacting motif. Left to Right: Panels showing the localization of RFP-Fib (magenta) and Pit-GFP (green) in Stage 16 embryo, RFP-HP1a (magenta) and Pit-GFP (green) in Stage 16 embryo, and Scarlet-I-HP1a (magenta) and Pit-mYFP (green) transiently transfected in S2R+ *Drosophila* cells. (**b**) Maximum intensity projections of Cycle 14, Cycle 17 and amnioserosa nuclei from +rDNA and -rDNA embryos showing RFP-HP1a (magenta) and Pit-GFP (green). Yellow arrows in -rDNA in Cycle 17 show the mixing of Pit and HP1a, while yellow arrows in -rDNA in cycle 17 and amnioserosa show the formation of the Pit neocondensate in the PCH void. (**c**) Time-lapse stills (single slices) of a -rDNA amnioserosa nuclei with RFP-HP1a (magenta) and Pit-GFP (green). (**d**) Mean intensity, (**e**) Circularity, and (**f**) Area of projections of Pitchoune in -rDNA embryos in amnioserosa nuclei. Mean of 35-60 nuclei at each time point in n=3 embryos. Error Bars: s.e.m. (**g**) Schematic summarizing nuclear organization phenotypes observed in +rDNA and -rDNA embryos.

302 **Pitchoune and its HP1a-interacting motif are required for PCH-nucleolar**
303 **associations**

304 Supported by our model and *in vivo* imaging, our findings indicate that Pitchoune is a
305 candidate amphiphile between PCH and nucleoli as a granular compartment nucleolar
306 protein with a lower affinity for PCH/HP1a. We next investigated the consequences of
307 removing Pitchoune on PCH-nucleolar associations. If Pitchoune regulates these
308 associations, we predicted that its depletion would disrupt the surrounding configuration.
309 We first tested this by decreasing the concentration of the amphiphilic protein in the
310 physical model while keeping all other parameters the same as in Fig. 4c. The simulations
311 revealed a progressive detachment of PCH from the nucleolus as Pitchoune levels
312 decreased (**Fig. 6a**). Note that in both simulations and *in vivo* experiments, even with the
313 loss of Pitchoune, nucleoli and PCH are expected to maintain a singular attachment at
314 the PCH-embedded rDNA locus. This is in contrast with the separation of Fibrillarin and
315 PCH observed in embryos lacking rDNA (**Fig. 2a, 4c**).

316 Next, we depleted Pitchoune using RNAi in the female germline (using a maternal GAL4
317 driver) to assess the impact of Pitchoune knockdown in *Drosophila* embryos. However,
318 ovary development was halted, and no eggs were laid following Pitchoune knockdown in
319 the female germline (**Extended Data Fig. 6a-b**), preventing further assessment of the
320 effects of Pitchoune knockdown in early embryos. These phenotypes align with the growth
321 defects observed in *pitchoune* homozygous mutants that die as small first instar larvae [39],
322 likely surviving early development due to maternal deposits of Pitchoune. Therefore, we
323 used eyeless-GAL4 to knock down Pitchoune in the eye-antennal discs of third-instar
324 larvae. Pitchoune knockdown severely disrupted the normal development of eye-antennal
325 discs (**Extended Data Fig. 6c**). Most importantly, viable cells displayed a 50% reduction
326 in the fraction of the nucleolar edge occupied by H3K9me2 after Pitchoune knockdown
327 (control RNAi mean = 0.296, Pitchoune RNAi mean = 0.146, p-value = 0.0011) (**Fig. 6b-**
328 **c**).

329 We also knocked down Pitchoune in S2R+ *Drosophila* cultured cells using RNAi,
330 achieving ~60% reduction in Pitchoune transcripts (**Extended Data Fig. 6d**). As
331 observed in eye discs, Pit knockdown decreased HP1a occupancy at the nucleolar edge
332 and disrupted its organization relative to the nucleolus, with ~50% reduction in HP1a
333 occupancy at the nucleolar edge, and a decrease in the percentage of nuclei displaying
334 the surrounded configuration (Mock RNAi: 87%, Pit RNAi: 27%) (**Fig. 6d-e, Extended**
335 **Data Fig. 6e-f**). These phenotypes were rescued by reintroducing full-length Pitchoune
336 (**Fig. 6e-f, Extended Data Fig. 6f**). We conclude that Pitchoune is important to establish
337 or maintain the surrounded configuration.

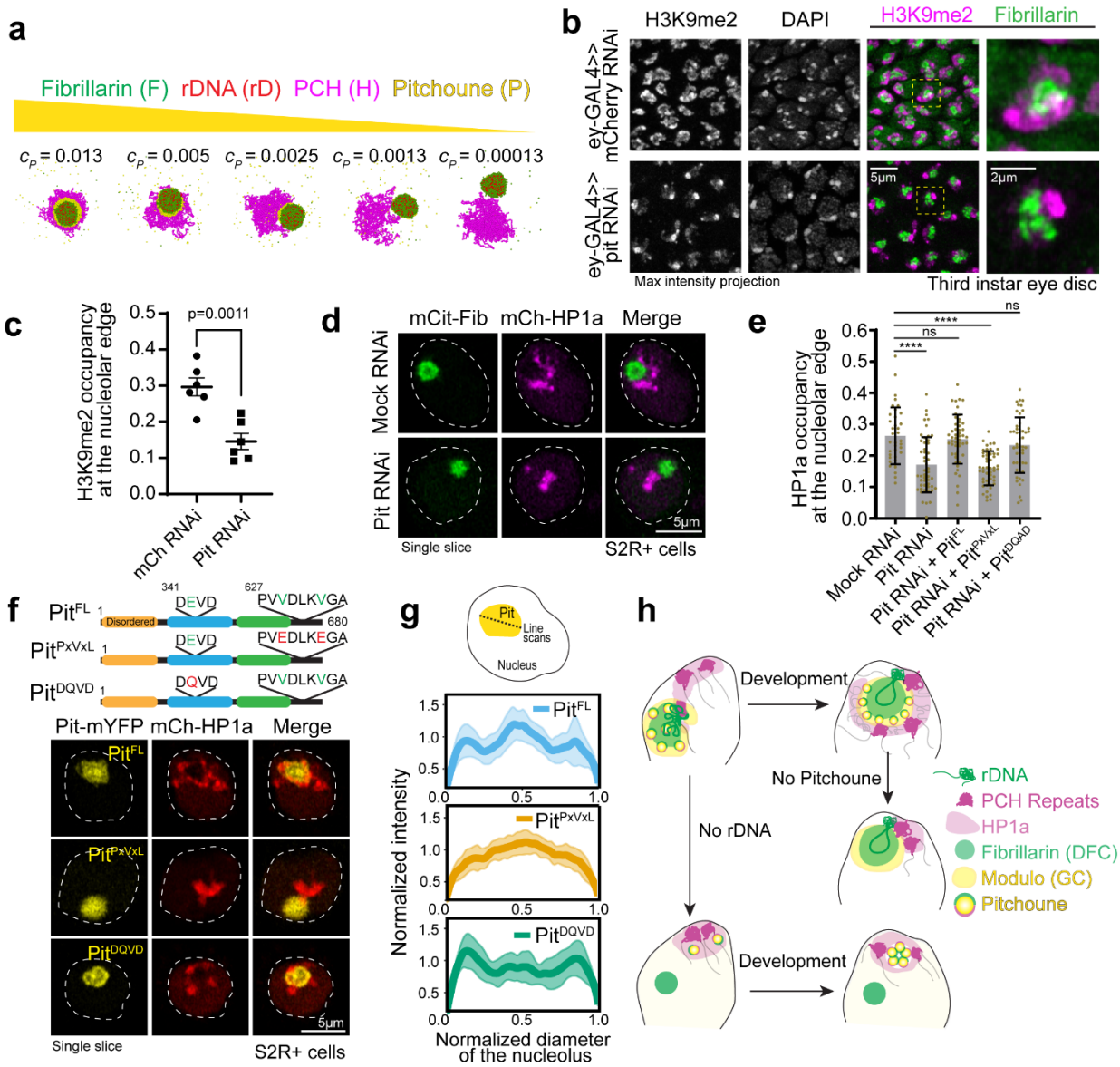

Fig. 6: Knockdown of Pitchoune or mutations in its HP1a-interaction motif disrupt PCH-nucleolar associations. (**a**) Simulation endpoint snapshots demonstrate how decreasing the concentration (c_P) of Pitchoune (P) (yellow) reduces the association of PCH (H) (magenta) around the Fibrillarin condensate (F) (green). (**b**) Immunofluorescence of H3K9me2 (magenta), Fibrillarin (green) and DAPI in nuclei from dissected eye-discs in third instar larvae from UAS-pit RNAi and UAS-mCherry RNAi (control) driven by the eyeless-GAL4 driver. (**c**) Quantification of the fraction of the nucleolar edge occupied by H3K9me2. Each data point indicates the mean value from one animal. n=6 animals with over 500 nuclei in total for each experimental group. Error bars: s.e.m. (**d**) Nuclei expressing Citrine-Fib and mCherry-HP1a transiently transfected after Pitchoune knockdown show decreased association of HP1a from the nucleolus. (**e**) Fraction of the nucleolar edge occupied by HP1a following Pit knockdown and rescue with Full length Pit (Pit^{FL}), Pit^{PxVxL} and Pit^{DQVD}. n=38-50 nuclei for each experimental group. Bar graphs show the mean ± s.d. (**f**) Schematic representation of Pitchoune mutations introduced: Pit^{PxVxL} contains mutations of the central valine (V) to glutamic acid (E) in the conserved PxVxL motifs. The putative helicase mutant is denoted as Pit^{DQVD}. Representative nuclei transfected with Pit^{FL}, Pit^{PxVxL}, and Pit^{DQVD} following RNAi-mediated knockdown of endogenous Pitchoune. (**g**) Line scans show Pitchoune distribution in the nucleolus of cells transfected with Pit^{FL} (n=25), Pit^{PxVxL} (n=37) and Pit^{DQVD} (n=40) after Pit RNAi. Intensities are normalized to the average value for each profile, and lengths are normalized to the diameter of the corresponding nucleolus. Solid line: mean, shaded error region: s.d. (**h**) Model for the organization of PCH (repeats and HP1a) around the nucleolus (rDNA, Fibrillarin and Modulo) via an amphiphilic linker Pitchoune during *Drosophila* development.

To determine the molecular basis of Pitchoune's 'amphiphilic' nature and test whether it is directly responsible for PCH-nucleolar associations, we investigated the roles of Pitchoune's conserved motifs in mediating these interactions. We disrupted the putative HP1a-interacting PxVxL motifs by mutating the two central valines (V) to glutamic acid (E) (Pit^{PxVxL}). The central V binds in a hydrophobic pocket at the interface of HP1 dimers, and mutating the hydrophobic V to the charged E residue disrupts their HP1 interaction [40]. We also generated a construct mutating the conserved DEVD motif in the Helicase domain to DQVD (Pit^{DQVD}) to block its Helicase activity [39,44] (**Fig. 6f**). Defects in HP1a organization relative to the nucleolus caused by Pit knockdown in S2R+ cells were rescued by transfection with full-length Pitchoune (Pit^{FL}) and Pit^{DQVD} but not Pit^{PxVxL} (**Fig. 6e-f)**. When expressing Pit^{FL} and Pit^{DQVD}, 73% and 62% of nuclei, respectively, exhibited the 'surrounded' PCH-nucleolar organization after Pit knockdown, compared to only 30% of nuclei expressing Pit^{PxVxL} (**Extended Data Fig. 6f**). Additionally, Pit^{PxVxL} showed uniform distribution in the nucleolus, unlike Pit^{FL} and Pit^{DQVD} which were enriched at the nucleolar edges (**Fig. 6f, g**). We conclude that the PxVxL motif regulates Pitchoune's sub-nucleolar distribution by promoting its enrichment at the nucleolar-PCH interface. Together, these experiments reveal the molecular basis of Pitchoune's amphiphilic function, showing that it promotes PCH-nucleolar associations through interactions with HP1a via its PxVxL motif.

Discussion

This study presents four main findings on the organization of PCH and nucleoli (**Fig. 6h**): (**1**) During early embryonic development, PCH-nucleolar associations are highly dynamic, transitioning from extended (nuclear edge-associated) to surrounded (nucleolar edge-associated) configurations (**Fig. 1**). (**2**) The nucleolus organizes PCH components in the 3D nuclear space, preventing PCH hyper-compaction (**Fig. 2**). (**3**) A hierarchy of interaction strengths between nucleolar and PCH components, including amphiphilic proteins with affinities for both, recapitulates the spatial organization seen in cells with and without nucleoli, and disrupting these hierarchies generates neo-condensates (**Fig. 3-5**). (**4**) Pitchoune and its C-terminal HP1a binding PxVxL motif are required for normal PCH-nucleolar associations (**Fig. 6**).

Sequence-based approaches have revealed that nuclear organization transitions from a naïve state to specific higher-order patterns during embryonic development [45]. However, these methods typically exclude the highly repetitive sequences that comprise most of the PCH and nucleoli, limiting our understanding of how PCH-nucleoli organization is established during development. Our study addresses this gap by visualizing PCH and nucleolar dynamics during *Drosophila* embryonic development in single nuclei at minute-scale resolution. Initially, PCH from different chromosomes undergo liquid-like fusions [19,21] to form a contiguous condensate that wraps around the nucleolus, explaining how PCH from chromosomes without rRNA genes is also positioned at the nucleolar edge. After

fusing into a contiguous condensate, PCH remains dynamic, transitioning from an 'extended' configuration in cycle 14 to a stable 'surrounded' state around the nucleolus in cycle 17. Transitions in heterochromatin organization reminiscent of the ‘extended’ intermediate have been observed during early embryonic development in *C. elegans* [46] and mice [47], suggesting similarities across species.

In its 'extended' intermediate state, PCH associates closely with the nuclear edge before repositioning around the nucleolus. This finding is intriguing because sequencing-based approaches have shown overlap between Nucleolus Associated Domains (NADs) and Lamin-Associated Domains (LADs) [24,48]. The molecular mechanisms behind this repositioning are unknown, but we speculate that PCH's affinity for the nuclear periphery decreases while its interaction strength with the nucleolus increases between cycles 14 and 17, with Pitchoune playing a crucial role. Post-translational modifications or increased concentrations of Pitchoune in cycle 17 might enhance its affinity for HP1a, correlating temporally with the stable surrounding of the nucleolus by HP1a in +rDNA and the appearance of the Pitchoune neo-condensate in -rDNA. Alternatively, the reduction in nuclear size during these developmental stages might cause a crowding effect, bringing PCH closer to the nucleolus. Changes in the volumes or molecular compositions of PCH and nucleolar condensates could also alter relative affinities or biophysical properties such as surface tension and viscosity. Future studies will reveal whether one or more of these mechanisms mediate the dynamic transitions in PCH-nucleolar association during early development.

An unexpected finding in this study was the reorganization of compacted heterochromatin into a toroid-like structure, with Pitchoune filling the core when rDNA was removed. This observation led us to propose the amphiphilic model of PCH-nucleolar organization. Pitchoune is a GC-localizing RNA helicase[39,43], has nucleolar localization signal motifs in its N-terminal tail [49], and its yeast ortholog is a ribosome assembly factor [50], altogether highlighting its dominant nucleolar affinity. We define Pitchoune's function as an amphiphile by demonstrating two key points: (i) it forms neo-condensates in the absence of rDNA, indicating self-association, and (ii) while Pitchoune does not stably mix with HP1a, it consistently shares an interface with HP1a in both its normal and neo-condensate forms suggesting a weak affinity for HP1a. This proximity is lost when the HP1a-interacting C-terminal PxVxL motif in Pitchoune is mutated. This gradient in interaction strengths creates a hierarchical organization and stabilizes PCH-nucleolar associations. Such a layering mechanism is distinct from the formation of nested subcompartments within the nucleolus, which are immiscible but associate due to sequential rRNA synthesis, processing and ribosome assembly [8,9,11] , however rRNA synthesis doesn't seem to be required for Pit-HP1a associations. While synthetic amphiphiles have been shown to generate multiphasic condensates both *in vitro* [38] and *in vivo* within stress granules [51], we demonstrate this mechanism in a natural context with

417 PCH and nucleoli and propose a generalizable role for amphiphilic molecules in co-
418 organizing immiscible condensates in cells.

419 How does Pitchoune compare to other molecules required for PCH clustering around the
420 nucleolus? For instance, depleting the Nucleoplasmin homolog NLP, CTCF, or Modulo in
421 *Drosophila* cultured cells [52] or NPM1 in human and mouse cell lines [53] causes the loss of
422 heterochromatin clustering around the nucleolar periphery. However, it is unclear if these
423 proteins play a direct role in PCH-nucleolar interactions or are required to form an intact
424 granular component that recruits other key factors. Similarly, loss of the surrounded
425 configuration upon depletion of Pitchoune protein in cultured cells or larval eye discs could
426 result from disrupting the composition or function of the granular component. However,
427 mutating only the key residues in Pitchoune's HP1a binding motif is sufficient to dissociate
428 PCH from the nucleolus, demonstrating that Pitchoune is directly responsible for binding
429 to HP1a and necessary for PCH-nucleolar associations. Nevertheless, a network of
430 structural and regulatory molecules may contribute to Pitchoune localization and the
431 overall affinity of PCH to the nucleolar edge. Proximity ligation or similar methods for
432 identifying a complete set of molecules enriched at the PCH-nucleolar interface will help
433 generate a full understanding of how Pitchoune promotes PCH associations and what
434 regulates the dramatic architectural changes in early development.

435 The composition of condensates is determined by the multivalency and binding affinities
436 of constituent molecules, and hierarchies in these properties can generate the higher-
437 order structure of multi-layered condensates [54,55]. Our findings demonstrate how
438 disrupting condensate nucleation sites or interaction hierarchies can form new, abnormal
439 nuclear structures or 'neocondensates' through inherent self-associations or secondary
440 interactions with other molecules. For example, loss of the nucleolus due to rDNA deletion
441 leads to PCH compaction, which resembles a collapsed polymer, likely due to increased
442 heterochromatin self-interactions. The specific responses of different components to
443 disruption likely reflect the types and relative strengths of their encoded interaction
444 modules. For instance, when rDNA is removed, Modulo is broadly dispersed throughout
445 the nuclear volume, likely due to its lack of self-association and affinity for other nuclear
446 structures. In contrast, Fibrillarin forms a separate spherical neocondensate when
447 deprived of its processing substrate rRNA, driven by strong self-association, and
448 Pitchoune, with strong self-association and a weak HP1a interaction motif, forms a
449 spherical neocondensate within the compacted PCH. Given the large number of multi-
450 component condensates within cells, it is crucial to assess whether new condensates
451 arise when perturbing interactions (e.g., by mutating a protein binding domain). Such
452 neomorphic responses, rather than the mutated protein itself, may cause defective
453 cellular phenotypes or behaviors. Understanding these outcomes will be important during
454 stress responses, aging, and cellular senescence when new condensates often form or
455 the composition of existing condensates changes [56].

Methods

Drosophila Stocks and Genetics

All crosses were maintained at 25° C. To visualize the dynamics of HP1a and nucleolar assembly, live embryos from *RFP-HP1a; GFP-Fib*, *RFP-Fib; GFP-HP1a* and *RFP-HP1a; GFP-Mod* stocks were imaged. Embryos lacking rDNA were obtained as described in Falahati et al. 2016 by crossing C(1)DX/Y; *RFP-HP1a; GFP-Fib* or C(1)DX/Y; *RFP-HP1a; Pit-GFP* or C(1)DX/Y; *RFP-Fib; Pit-GFP* virgins to C(1;Y)6,y[1]w[1]f[1]/0 males. 1/4th of the resulting embryos from this cross lack rDNA, and -rDNA embryos were selected based on the presence of Fibrillarin neocondensates in live and fixed embryos and DAPI morphology in fixed embryos. To knockdown Pitchoune in eye discs, eyeless-GAL4 virgin females were crossed with Pitchoune RNAi VAL20 males, and eye discs were dissected from F1 third instar larvae.

Fly Genotype	Source
RFP-HP1a (2nd Chr)	Lipsick Lab (Wen et al., 2008)
GFP-HP1a (3rd Chr)	Lipsick Lab (Wen et al., 2008)
GFP-Fibrillarin	Weischaus Lab (Falahati and Wieschaus, 2017)
RFP-Fibrillarin	Weischaus Lab (Falahati et al., 2016)
GFP-Modulo	Weischaus Lab (Falahati and Wieschaus, 2017)
Pitchoune-GFP	Weischaus Lab (Falahati and Wieschaus, 2017)
FM6/C(1)DX, y[*] f[1]	BDSC # 784
C(1)RM/C(1;Y)6,y[1]w[1]f[1]/0	BDSC # 9460
Mat alpha GAL4	BDSC # 7063
Eyeless-GAL4	BDSC # 5534
Pitchoune RNAi VAL20	BDSC # 80368
Pitchoune RNAi VAL22	BDSC # 43984

Preparing *Drosophila* embryos for live imaging

To collect *Drosophila* embryos for live imaging, males and females of the desired genotype were added to a plastic cage covered with apple juice agar plates and left for at least 3 days at 25°C. On the day of imaging, a fresh plate was added to the cage, and embryos were collected for two hours. After removing the plate, embryos were coated with Halocarbon oil 27 (Sigma) for staging using a dissection scope with transillumination. Stage-selected embryos were placed on a 2 x 2 inch paper towel square and dechorionated in 50% bleach for 1 min. Bleach was wicked off with a Kimwipe after 1 min, the square was washed with a small amount of distilled water, and excess water was wicked off. Dechorionated embryos were secured onto a semipermeable membrane (Lumox film, Starstedt) on a membrane slide holder using Heptane Glue. These embryos were mounted in Halocarbon oil 27 (Sigma) between the membrane and a coverslip.

493 **Immunostaining**
494 Embryos were collected on apple juice-agar plates and aged till the appropriate stage,
495 dechorionated in 50% bleach, fixed in 1:1 heptane:4% formaldehyde (Sigma) in 1XPBS
496 for 25 mins, devitellinized in a 1:1 mixture of methanol:heptane, and stored at -20°C in
497 methanol. Embryos were rehydrated by washing in 1xPBS+0.2% Triton (PBT). Dissected
498 eye-discs were fixed in 4% formaldehyde in PBS for 20min, and the fixative was washed
499 with PBT. Following washes with PBT, tissues were blocked for ~1hr with 2% BSA in PBT,
500 then incubated with the primary antibody at 4°C overnight. After incubation with the
501 appropriate secondary antibody at room temperature for 2 hrs, samples were stained in
502 DAPI and mounted onto a slide using VectaShield (Vector Laboratories) mounting
503 medium. All primary antibodies were used at 1:250 dilution and secondaries at 1:1000.
504 Primary antibodies: Rabbit anti-Fibrillarin (Abcam ab5821), Mouse anti-H3K9me2
505 (Abcam ab1220), Rabbit anti-H3K9me3 (Abcam ab8898), Mouse anti-Modulo (Gift from
506 Mellone Lab, from Chin-Chi Chen et al., 2012), Mouse anti-Lamin, Dm0 (DSHB
507 ADL67.10). Secondary antibodies: Goat-anti-Mouse, Alexa Fluor 488 (Invitrogen A-
508 11001), Goat-anti-Mouse, Alexa Fluor 568 (Invitrogen A-11004), Goat-anti-Rabbit, Alexa
509 Fluor 488 (Invitrogen A-11034), Donkey-anti-Rabbit, Alexa Fluor 568 (Invitrogen A-
510 10042).

511 **DNA Fluorescent in situ hybridization (FISH) and combined Immuno-FISH**
512 Probe Labelling
513 A probe for ITS-1 rDNA was prepared by amplifying an ~800 bp fragment by PCR from
514 genomic DNA using the primers 5'-ACGGTTGTTTCGCAAAAGTT-3' and 5'-
515 TGTTGCGAAATGTCTTAGTTTCA-3', cloned into a pGEM T-Easy vector (Promega) and
516 used as a template for probe synthesis. ITS-1 rDNA probe was labeled with Alexa 488,
517 Alexa 555, or Alexa 648 using the FISH Tag™ DNA Multicolor Kit (ThermoFisher)
518 following the manufacturer's protocol. Locked nucleic acid (LNA) oligonucleotides
519 (Integrated DNA technologies) conjugated with Cy5 or FAM were used as probes for
520 359bp, 1.686, and AAGAG satellite DNA repeats.

521 Hybridization
522 Embryos were collected on apple juice-agar plates and aged till the appropriate stage,
523 dechorionated in 50% bleach, then fixed in 1:1 heptane: 4% formaldehyde in 1XPBS for
524 25 mins, devitellinized in a 1:1 mixture of methanol: heptane, and stored in -20°C.
525 Embryos were washed in 2xSSC-T (2xSSC containing 0.1% Tween-20) with increasing
526 formamide concentrations (20%, 40%, then 50%) for 15 min each. 100ng of DNA probes
527 in 40 µl of hybridization solution (50% formamide, 3× SSCT, 10% dextran sulfate) was
528 added, denatured together with the embryos at 95°C for 5 min and incubated overnight
529 at 37°C. Following hybridization, embryos were washed twice in 2xSSCT for 30 mins at
530 37°C and thrice in PBT for 5 mins at room temperature. After completing washes, embryos

531 were stained in DAPI and mounted onto a slide using VectaShield (Vector Laboratories)
532 mounting medium.

533 Combined Immuno-FISH
534 Immunofluorescence was performed first on embryos for combined in situ detection of
535 proteins and DNA sequences. Embryos were post-fixed in 4% formaldehyde for 25 mins,
536 then processed for FISH.

537 **Pan-Protein Staining using 488 NHS Ester**
538 Formaldehyde-fixed embryos were devitellinized in a 1:1 mixture of methanol: heptane
539 and stored in methanol. Embryos were rehydrated by washing in 1xPBS+0.2% Triton
540 (PBT). After washing off methanol, embryos were stained in the diluted Atto 488 NHS
541 ester fluorophore (Sigma) (1:50) from a 10mg/ml stock in 0.1% PBST for 6 h at 4 °C
542 followed by washing in PBT three times for 30 mins each at room temperature. Embryos
543 were stained in DAPI for ten minutes and mounted onto a slide using VectaShield (Vector
544 Laboratories) mounting medium.

545 **Propidium Iodide Staining**
546 Formaldehyde-fixed and Heptane devitellinized embryos were rehydrated by washing in
547 1xPBS+0.2% Triton (PBT). Samples were equilibrated in 2X SSC. RNase-treated controls
548 alone were incubated in 100 µg/mL DNase-free RNase in 2X SSC for 20 minutes at 37°C.
549 After washing away the RNase with 2X SSC, embryos were incubated in 500nM of
550 Propidium Iodide (Invitrogen) in 2X SSC for 10 mins at room temperature. Samples were
551 rinsed in 2X SSC, stained with DAPI, and mounted on a slide with VectaShield (Vector
552 Laboratories) mounting medium.

553 **Microscopy**
554 Imaging was performed on a Zeiss LSM880 Airy Scan microscope (Airy Fast mode) with
555 a 63X NA 1.4 oil immersion objective at room temperature. Depending on the fluorophore,
556 405, 488, 514, or 633nm laser lines were used for excitation with appropriate filter sets.
557 Laser intensity values, detector gain, image size, zoom, z-stack intervals, and time
558 intervals (for time-lapse acquisitions) were adjusted to minimize bleaching and ensure
559 uniform detection across all AiryScan detection elements. Once standardized for an
560 experiment, settings were kept identical across all samples in the experimental groups.
561 Raw images were processed using Zeiss ZEN Black software with the AiryScan
562 processing module for reconstruction and subsequent image analysis.

563 **Modeling**
564 To better understand the association of PCH with the nucleolus, we developed a physical
565 model that simulates the interactions between different types of molecules found in these
566 biomolecular condensates. In our physical model, we simulate four components of the
567 nucleus: PCH (H) and ribosomal DNA (rD) as long polymers, and Fibrillarin (F) and an
568 amphiphilic protein (X) as independent, single monomers, which we hereafter refer to as

beads. Since the experiments focused on the PCH domain of *Drosophila*, our physical model only simulates this specific region of the genome (30% of the genome), not the entire genome. This allows us to study the dynamics of this particular region of the genome more accurately and efficiently. PCH is modeled as a semiflexible bead-spring polymer chain in which N beads are connected by N-1 harmonic springs. Each bead of the chain represents a cluster of PCH containing approximately 5 kilo base pairs of DNA, with a diameter of approximately 30 nm. The semi-flexibility of the chain is determined by its persistence length, which is taken to be 60 nm (2 beads) in accordance with previous studies that indicate chromatin has a persistence length between 50 to 100 nm (Wachsmuth et al. 2016). We represent rDNA as a self-avoiding chain that occupies approximately 20% of the middle domain of PCH. Fibrillarin and the amphiphilic protein X are modeled using single, diffusive beads where each protein has distinct interactions with the polymer and other proteins.

To simplify the model, we assume that the size of each protein bead is equal to the size of the heterochromatin bead, with both having a diameter σ. The non-bonding interactions between polymer-polymer, protein-protein, and polymer-protein are modeled using a standard Lennard-Jones (LJ) potential. The LJ potential is truncated at the distance 2.5 σ, meaning that the interaction between the beads is only non-zero if they are within 2.5 σ distance. At very short distances between the beads, the LJ potential is strongly repulsive (representing the excluded volume of two molecules). At intermediate spacings, the LJ potential is attractive, with a strength adjusted to model the different states of chromatin, such as its compaction or decondensation and the phase-separating tendency of the proteins. In our model, the polymer and the proteins are confined within a spherical boundary that represents the nucleus of the cell. This boundary mimics the effect of the nuclear envelope, which constrains the movement of these beads and affects their interactions with each other. In our study, we used the LAMMPS (Large-scale Atomic/Molecular Massively Parallel Simulator) package to simulate the behavior of our biomolecular system (Thompson et al. 2022). LAMMPS uses Brownian dynamics, which accounts for the viscous forces acting on the beads, and a stochastic force (Langevin thermostat) to ensure that the system of beads and solvent is maintained at a constant temperature (NVT ensemble). This allows us to model the interactions between polymer-polymer, polymer-protein, and protein-protein beads accurately and study the behavior of the system over time.

Rationale for the choice of parameters in the coarse-grained model

To analyze the experimental observations of phase separation in the nucleus, we study a minimal model with four crucial components: PCH (H), rDNA (rD), Fibrillarin (F), and an amphiphilic protein (X) that binds both nucleolar and PCH components. The parameters in the simulations include the number of molecules of each component α (N_α), the strength of the attractions between two components (denoted by indices β and γ, $\epsilon_{\beta\gamma}$),

and the size of the confinement (R_c). The fraction of the nucleus that is hydrated (does not contain PCH or the other proteins) is obtained from the relative difference between the confinement volume and the volumes of PCH and the other proteins.

<u>Bonding potential between monomers in the polymer made of PCH and rDNA:</u> Adjacent beads on the polymer chain are interconnected by harmonic springs using the potential function:

$$V_s = \sum_{i=1}^{N-1} k_s (r_i - \sigma)^2$$

Here, r_i represents the distance between the i-th and $(i+1)$-th beads. The spring constant and equilibrium distance between neighboring beads are denoted as k_s and σ respectively. In our simulations, the spring constant k_s is set to $\frac{100\, k_B T}{\sigma^2}$ to ensure the presence of rigid bonds between adjacent beads of the polymer chain.

<u>Attraction strength ($\epsilon_{\beta\gamma}$)</u>: The Lennard-Jones potential is used to model the attraction between any two non-bonded beads:

$$V_{\beta\gamma}(r) = 4\epsilon_{\beta\gamma}\left[\left(\frac{\sigma}{r}\right)^{12} - \left(\frac{\sigma}{r}\right)^{6}\right] \text{ for } r \leq r_c \text{ and 0 for } r \leq r_c$$

Here, the symbol $\epsilon_{\beta\gamma}$ represents the attraction strength between beads of type β and γ, where $\beta, \gamma \in \{H, rD, F, X\}$ represent PCH, rDNA, Fibrillarin, and amphiphilic protein, respectively. For instance, ϵ_{FX} represents the attraction strength between Fibrillarin and amphiphilic protein beads. When dealing with attractive interactions between chromatin-chromatin and chromatin-protein beads, a distance cutoff of $r_c = 2.5\sigma$ is used for the Lennard-Jones potential, beyond which the interaction is set to zero. To account for only excluded volume interactions (with no attractions) using the same potential, a cutoff of $r_c = 2^{1/6}\sigma$ and $\epsilon = 1k_BT$ are employed. This choice is made because the potential energy is at its minimum at that point, and the resulting force on a bead is zero. As there are four components in our model, there are a total of 10 combinations (n(n+1)/2), where n is number of components, of attraction strength parameters between the different components.

<u>Confinement size:</u> The size of the confinement is determined by defining the volume fraction of chromatin ϕ:

$$\phi = N_G \times \frac{\text{volume of 1 bead}}{\text{volume of confinement}} = N_G \times \frac{(\frac{4}{3}\pi\sigma^3)}{(\frac{4}{3}\pi R_c^3)}$$

637 Here, N_G represents the total number of beads in the *Drosophila* genome, where each
638 bead corresponds to 5 kilobase pairs (kbps) of DNA. The diameter of a spherical bead,
639 denoted as σ, is taken to be 30 nm (see [59] for further explanation). The total length of the
640 diploid *Drosophila* genome is 360 Mbps, and N_G can be calculated by dividing the
641 *Drosophila* genome length by the amount of DNA represented by one bead (5 kbps). The
642 volume fraction of chromatin (ϕ) is commonly reported as ~ 0.1 in existing literature (Qi
643 & Zhang, 2021; Tripathi & Menon, 2019). Using the equation above, the calculated radius
644 of the confinement (R_c) is found to be 45σ.

645 <u>Number of molecules in PCH and rDNA:</u> We model the PCH domain as a polymer chain
646 composed of $N = 10{,}000$ beads, which represents approximately 30% of the beads in the
647 entire genome. Among these $10{,}000$ beads, 20% are designated as rDNA, resulting in a
648 total of $4{,}000$ rDNA beads. We do not explicitly model the rest of the genome since the
649 experiments show that the nucleolar components are localized near PCH.

650 <u>Concentration of Fibrillarin and amphiphilic protein:</u> The concentration of Fibrillarin and
651 amphiphilic protein is calculated as follows:

652 $$\text{concentration } (c_\alpha) = \frac{N_\alpha}{\text{volume of confinement}}$$

653 Here, the symbol α represents the type of protein, where $c_\alpha = c_F$ for the fibrillarin
654 concentration and $c_\alpha = c_X$ for the amphiphilic protein concentration. After defining the
655 parameters and obtaining the value for the confinement radius parameter from the
656 assumed volume fraction of PCH, we proceed with an initial simulation, focusing on a
657 single component, namely the Fibrillarin protein, within the confinement. During this
658 simulation, we vary the concentration (c_F) and the attraction strength (ϵ_{FF}) of Fibrillarin.
659 Our experimental results demonstrate that Fibrillarin undergoes phase separation
660 independently of the other components (rDNA or PCH) during cycle 14 (refer to Figure
661 2A). These initial-stage simulation results yield a phase diagram, which indicates that a
662 minimum attraction strength of $1.3 - 2.0 k_{\mathrm{B}}\mathrm{T}$ is required to condense fibrillarin particles
663 within the concentration range of $c_F = 0.0013 - 0.013$. The reported concentration of
664 nucleolar particles is $c = 0.015$ (Qi & Zhang, 2021). Consequently, we maintain a fixed
665 concentration of Fibrillarin at $c_F = 0.013$ when simulating all the other protein components
666 (**Extended Data Fig. 4a**). Since the concentration of amphiphilic protein is not determined
667 from the experiments, we conducted multiple simulations, systematically varying the
668 amphiphilic protein concentration (c_X) within the range of $0.0013 - 0.13$. The results of
669 these simulations are discussed in **Fig. 6a-b**.

670 <u>Parameter range of ϵ_{HH}</u>: To understand the behavior of each component separately
671 (before including interactions between different components) in the next stage, we
672 conducted simulations specifically focusing only on the PCH chain. The PCH chain
673 represents a condensed chromatin region within the nucleus which implies self-attractive

interactions of the beads representing the polymer. During these simulations, we varied the attraction strength between PCH beads (ϵ_{HH}) from 0 to $0.5k_{\mathrm{B}}$T. Our results revealed that within the range of $\epsilon_{HH} = 0.35 - 0.5\ k_{\mathrm{B}}$T (**Extended Data Fig. 4b**), the PCH chain underwent collapse, resulting in a condensed conformation that is phase-separated from the aqueous component of the system (not simulated explicitly).

Parameter value of ϵ_{rD-F}: We next simulate the self-organization due to the interactions between the three components (where each component so far was considered alone): PCH, rDNA, and Fibrillarin. We set $\epsilon_{HH} = 0.35\ k_{\mathrm{B}}$T and $\epsilon_{FF} = 2\ k_{\mathrm{B}}$T, incorporating only excluded-volume interactions (hard-core, repulsive interactions) between H-F, i.e., there is no direct attraction between PCH and Fibrillarin as implied by the experiments. By varying the attraction strength between rDNA and Fibrillarin (ϵ_{rD-F}), we made the following observations based on our simulation results: a weaker attraction (and $\epsilon_{rD-F} = 0.75\ k_{\mathrm{B}}$T) resulted in rDNA wrapping around the condensed Fibrillarin phase, while a stronger attraction (and $\epsilon_{rD-F} = 2\ k_{\mathrm{B}}$T) led to the condensation of rDNA within the Fibrillarin complex. This latter observation aligns with our experimental findings. Therefore, we select $\epsilon_{rD-F} = 2\ k_{\mathrm{B}}$T as the parameter value in the subsequent simulations (**Extended Data Fig. 4c**).

Parameter ranges of ϵ_{FF} and ϵ_{XX}: Finally, we introduce the fourth component, an amphiphilic protein 'X', which we suggest may interact attractively with both PCH and Fibrillarin. Initially, we investigated the relative attraction strengths between Fibrillarin and protein X when considering the same concentration for both. We explore all possible combinations of ϵ_{FF} both greater than and less than ϵ_{XX}. For $\epsilon_{XX} \geq \epsilon_{FF}$, we observe PCH surrounding the amphiphilic protein-rich phase, but just a partial wetting between the amphiphilic protein-rich phase and the Fibrillarin-rich phase (**Extended Data Fig. 4d**). Only when $\epsilon_{XX<}\epsilon_{FF}$ do we observe PCH surrounding the amphiphilic protein-rich phase, which in turn surrounds the Fibrillarin condensate, consistent with the experimental results in wild type embryos.

Parameter range of ϵ_{FX}: We proceeded to vary the attraction strength between Fibrillarin and amphiphilic protein X within the range of $\epsilon_{FX} = 1.5k_{\mathrm{B}}$T. When the attraction strength is relatively low ($\epsilon_{FX} \leq 0.75k_{\mathrm{B}}$T), the fibrillarin-rich phase and the amphiphilic protein-rich phase do not associate with each other. At moderate attraction strengths ($\epsilon_{FX} \geq 1k_{\mathrm{B}}$T and ($\epsilon_{FX} \leq 1.25k_{\mathrm{B}}$T), the Fibrillarin-rich and amphiphilic protein-rich phases partially wet each other. Finally, at higher attraction strengths ($\epsilon_{FX} = 1.5k_{\mathrm{B}}$T), the amphiphilic protein completely wets Fibrillarin (**Extended Data Fig. 4e-f**).

Parameter range of c_X: Additionally, we explored variations in the concentration of amphiphilic protein X (c_X). Notably, for higher concentrations of protein X ($c_X = 0.005 - 0.013$), we observed that heterochromatin tends to completely engulf the amphiphilic protein-rich phase, which in turn engulfs Fibrillarin (**Fig. 6a**).

712 **Cell culture**

713 *Drosophila* S2 cells were cultured in Schneider's *Drosophila* Medium (Gibco) with 10%
714 FBS and 1% antibiotic-antimycotic (Gibco) at 25°C. For transfections, cells were seeded
715 at 5 x 10^5 cells/mL in 6-well plates 24 hours prior. 1 µg of plasmid DNA was diluted in 100
716 µL of serum-free medium and mixed with 2 µL of TransIT-2020 Transfection Reagent
717 (Mirus Bio). After a 15-min incubation, the DNA-reagent complexes were added to the
718 cells and incubated at 25°C for 48-72 hours before visualizing.

719 **Plasmids/Recombinant DNA**

720 Codon-optimized gene blocks for Pitchoune, Fibrillarin, Modulo, Polr1E, and HP1a were
721 synthesized by Twist Biosciences and cloned into pCOPIA vectors fused with fluorescent
722 protein tags. Site-directed mutagenesis was performed to introduce PxVxL and DQVD
723 mutations into the full-length Pitchoune using the Q5® Site-Directed Mutagenesis Kit
724 (New England Biolabs) using these primers:

Pit^{PxVxL}_F: CCGGTAGAAGATCTCAAAGAAGGAGCTGCTAAGCG
Pit^{PxVxL}_R: CGGTACCAGGAAGCCGAAAC
Pit^{DQVD}_F: CCAAGTCGACAGGATCCTGG
Pit^{DQVD}_R: TCGATGATGAGGCACTGCAA

725 **Pitchoune RNAi**

726 Genomic DNA from S2 cells was used as the template for PCR amplification with the
727 primers listed below to generate the amplicon for Pitchoune RNAi targeting its 3'
728 untranslated region (3'UTR). Mock RNAi targeting the y gene was used as a negative
729 control.

T7-Pit-RNAi-F: TAATACGACTCACTATAGGgctgctttacttgagtgtgtgt
T7-Pit-RNAi-R: TAATACGACTCACTATAGGccaaggtggcccgcaattat
T7-Mock-RNAi-F: TAATACGACTCACTATAGGgaaaaactaagccaacgtcatc
T7-Mock-RNAi-R: TAATACGACTCACTATAGGgccgtggatataggcaaaaa

730 Hi-Scribe T7 Synthesis kit (New England Biolabs) was used to synthesize double-
731 stranded RNA (dsRNA) using manufacturer's protocol. Following synthesis, RNA
732 purification was carried out utilizing the MinElute RNeasy Kit (Qiagen). The purified RNA
733 was then diluted to 1 µg/µl. For the RNAi experiment, 3-5 µg of dsRNA with DOTAP
734 liposomal transfection reagent (Roche) was used per 0.5 x 10^6 cells. Cells were
735 analyzed 5 or 6 days after the initiation of RNAi.

736 **Total RNA Preparation, cDNA Synthesis, and Quantitative PCR**
737 Total RNA from S2R+ cells was extracted by homogenizing in TRIzol Reagent
738 (Invitrogen). 0.5 volume of chloroform was added, the mixture was shaken for 15
739 seconds, incubated for 3 minutes, and centrifuged at 12,000 x g for 15 minutes at 4°C.
740 The aqueous phase was transferred to a new tube, mixed with 500 µL of isopropanol,
741 incubated for 10 minutes, and centrifuged at 12,000 x g for 10 minutes at 4°C. The RNA
742 pellet was washed with 75% ethanol, centrifuged at 7,500 x g for 5 minutes at 4°C, air-
743 dried for 5-10 minutes, and resuspended in RNase-free water. Total RNA was treated with
744 DNA-free DNA removal kit (Invitrogen) per manufacturer's protocol to remove any
745 contaminating genomic DNA. RNA was converted to cDNA with GoScript Reverse
746 Transcriptase Kit (Promega) using random primers, and Real-Time PCR was performed
747 using PerfeCTa SYBR® Green FastMix (Quantabio) on the Biorad CFX96 Real-Time PCR
748 Detection system. Analysis was performed using the $2^{-\Delta\Delta Ct}$ method, with relative mRNA
749 levels of Pitchoune normalized to β-actin.

750 **Quantitative Image Analysis**
751 3D measurements were performed using Arivis Vision4D (Zeiss) while ImageJ was used
752 for all 2D measurements. The details of each analysis pipeline used in this study are listed
753 below:
754 Measuring the fraction of the nucleolar edge occupied by HP1a or H3K9me2
755 Fig. 1c: Nuclei were manually chosen for analyses ~15-30 mins into the specified
756 interphase and defined as "Early Cycle ", while those observed from ~50-70 mins were
757 defined as "Late Cycle ". Preprocessing steps include background subtraction and
758 denoising using Gaussian blur. HP1a and Fibrillarin were segmented in 3D using the
759 "Intensity Threshold Segmenter" with the Auto segmentation method. To calculate HP1a
760 occupancy at the nucleolar edge, the nucleolus was dilated by 1 pixel and subtracted
761 from the dilated object to create a 1-pixel shell around the nucleolus. The nucleolus shell
762 was intersected with HP1a segments to calculate the volume fraction of the nucleolar
763 shell that overlaps with HP1a.
764 Fig. 6c: Same as above, except the nucleolus was dilated by 2 pixels to create a
765 2-pixel shell around the nucleolus. The shell was intersected with H3K9me2 segments in
766 nuclei from eye-discs to calculate the fraction of the nucleolar shell that overlaps with
767 H3K9me2.
768 Fig. 6e: Same as above, except the nucleolus was dilated by 4 pixels to generate
769 a 4-pixel shell around the nucleolus. The thickness of the nucleolar shell scaled with
770 nucleolar size in the different cell types.

771 Measuring Distances
772 Fig. 2b: HP1a and Fibrillarin were segmented using the "Intensity Threshold
773 Segmenter" with the Auto segmentation method. The distance between HP1a and its
774 nearest Fibrillarin segment was measured in 3D using the "Distances" feature in Arivis.

Fig. 2f: AAGAG and 1.686 were segmented using the "Intensity Threshold Segmenter" with the Auto segmentation method. The distance between AAGAG and its nearest 1.686 segment was measured in 3D using the "Distances" feature in Arivis.

Extended Data Fig. 2e: Preprocessing steps include background subtraction and denoising using Gaussian blur. 1.686 or 359bp foci and Fibrillarin were manually segmented using the "Intensity Threshold Segmenter" with the Simple segmentation method. The distance between a Fibrillarin segment and its nearest 1.686 or 359bp locus was measured in 3D using the "Distances" feature in Arivis.

Measuring Aspect Ratio of HP1a

Fig. 2d: Individual nuclei were manually selected 15 mins after the start of Cycle 15. Preprocessing steps include background subtraction and denoising using Gaussian blur. HP1a was segmented using Auto thresholding using Otsu. The aspect ratio of the segment was determined using the Analyze Particles feature in Fiji.

Line Scans:

Fig. 6g: Nucleoli were segmented in Fiji using Otsu's method. The Feret's diameter was calculated for each nucleolus, and intensity values were measured along the Feret's diameter. Intensities for each profile were normalized to its average value. The Feret's diameter was normalized by setting its range from 0 to 1.

Pitchoune neo-condensate formation measurements

Fig. 5d-f: To measure the dynamics of the formation of Pitchoune in -rDNA embryos, maximum intensity projections of Amnioserosa were first preprocessed in Fiji using Subtract background and a Gaussian Blur filter. Auto thresholding for each time point was performed using the Yen method. Using Analyze Particles, the area, circularity, and mean intensity of each segment of Pitchoune was extracted. The mean intensity over time was normalized to its value at T=0.

Statistical Analysis

Data were plotted, and statistical analyses were performed using GraphPad Prism8. P-values were calculated using unpaired two-tailed t-tests.

Data availability statement

All data supporting the results of this study are included in the manuscript. Reagents used in this study are available upon request.

Code availability statement

For the simulation component of this study, all simulations, analyses, and visualizations were conducted using publicly available software packages and custom-developed codes. Langevin Dynamics simulations were performed using LAMMPS (version 23 June 2022), and visualizations were generated using Ovito (version 3.7.11). The complete set of codes required to reproduce the simulations is available in the following

repository: https://github.com/gauravbajpaimaths/Coarse-grained_model_of_nucleolar_heterochromatin_condensates

ACKNOWLEDGEMENTS

We thank Eric Weischaus (Princeton University) for generously sharing the fluorescently tagged nucleolar fly lines. The Karpen lab acknowledges critical support from the National Institutes of Health (R35GM139653), and SS and GHK are grateful for the support of the Volkswagen Stiftung (98196).

AUTHOR CONTRIBUTIONS

SR: conceptualization, experimentation, data acquisition, formal analysis, validation, investigation, methodology, and writing
OA: conceptualization, investigation, formal analysis, and writing
GB: simulations, data acquisition, formal analysis, methodology, and writing
KL: experimentation and data acquisition
SC: experimentation, data acquisition, reagent preparation, and formal analysis
SS: writing, funding acquisition, and supervision
GHK: conceptualization, writing, funding acquisition, and supervision

COMPETING INTERESTS

No competing interests to declare.

BIBLIOGRAPHY

1. Strom, A. R. & Brangwynne, C. P. The liquid nucleome – phase transitions in the nucleus at a glance. *J Cell Sci* **132**, jcs235093 (2019).

2. Misteli, T. The Self-Organizing Genome: Principles of Genome Architecture and Function. *Cell* vol. 183 Preprint at https://doi.org/10.1016/j.cell.2020.09.014 (2020).

3. Shin, Y. & Brangwynne, C. P. Liquid phase condensation in cell physiology and disease. *Science (1979)* **357**, eaaf4382 (2017).

4. Lyon, A. S., Peeples, W. B. & Rosen, M. K. A framework for understanding functions of biomolecular condensates on molecular to cellular scales. *Nat Rev Mol Cell Biol* **22**, 215 (2021).

5. Ditlev, J. A., Case, L. B. & Rosen, M. K. Who's In and Who's Out—Compositional Control of Biomolecular Condensates. *J Mol Biol* **430**, 4666–4684 (2018).

6. Fare, C. M., Villani, A., Drake, L. E. & Shorter, J. Higher-order organization of biomolecular condensates. *Open Biol* **11**, 210137 (2021).

7. Pederson, T. The nucleolus. *Cold Spring Harb Perspect Biol* **3**, 1–16 (2011).

8. Feric, M. *et al.* Coexisting Liquid Phases Underlie Nucleolar Subcompartments. *Cell* **165**, 1686–1697 (2016).

9. Lafontaine, D. L. J., Riback, J. A., Bascetin, R. & Brangwynne, C. P. The nucleolus as a multiphase liquid condensate. *Nat Rev Mol Cell Biol* **22**, 165–182 (2020).

10. Riback, J. A. *et al.* Composition-dependent thermodynamics of intracellular phase separation. *Nature 2020 581:7807* **581**, 209–214 (2020).

11. King, M. R. *et al.* Macromolecular condensation organizes nucleolar sub-phases to set up a pH gradient. *Cell* **187**, 1889-1906.e24 (2024).

12. Padeken, J. & Heun, P. Nucleolus and nuclear periphery: Velcro for heterochromatin. *Curr Opin Cell Biol* **28**, 54–60 (2014).

13. Bizhanova, A. & Kaufman, P. D. Close to the edge: Heterochromatin at the nucleolar and nuclear peripheries. *Biochim Biophys Acta Gene Regul Mech* **1864**, 194666 (2021).

14. Janssen, A., Colmenares, S. U. & Karpen, G. H. Heterochromatin: Guardian of the Genome. *Annu Rev Cell Dev Biol* **34**, 265–288 (2018).

15. Politz, J. C. R., Scalzo, D. & Groudine, M. Something Silent This Way Forms: The Functional Organization of the Repressive Nuclear Compartment. *Annu Rev Cell Dev Biol* **29**, 241–270 (2013).

16. Eissenberg, J. C. & Elgin, S. C. The HP1 protein family: getting a grip on chromatin. *Curr Opin Genet Dev* **10**, 204–210 (2000).

17. Keenen, M. M. *et al.* HP1 proteins compact DNA into mechanically and positionally stable phase separated domains. 1–30 (2020).

866 18. Larson, A. G. *et al.* Liquid droplet formation by HP1α suggests a role for phase separation
867 in heterochromatin. *Nature* **547**, 236–240 (2017).

868 19. Strom, A. R. *et al.* Phase separation drives heterochromatin domain formation. *Nature*
869 **547**, 241–245 (2017).

870 20. Wang, L. *et al.* Histone Modifications Regulate Chromatin Compartmentalization by
871 Contributing to a Phase Separation Mechanism. *Mol Cell* 1–14 (2019)
872 doi:10.1016/j.molcel.2019.08.019.

873 21. Tortora, M. M. C., Brennan, L. D., Karpen, G. & Jost, D. HP1-driven phase separation
874 recapitulates the thermodynamics and kinetics of heterochromatin condensate formation.
875 *Proc Natl Acad Sci U S A* **120**, (2023).

876 22. McClintock, B. The relation of a particular chromosomal element to the development of
877 the nucleoli in Zea mays. *Zeitschrift für Zellforschung und Mikroskopische Anatomie* **21**,
878 294–326 (1934).

879 23. Quinodoz, S. A. *et al.* Higher-Order Inter-chromosomal Hubs Shape 3D Genome
880 Organization in the Nucleus. *Cell* **174**, 744-757.e24 (2018).

881 24. Bersaglieri, C. *et al.* Genome-wide maps of nucleolus interactions reveal distinct layers of
882 repressive chromatin domains. *Nature Communications 2022 13:1* **13**, 1–18 (2022).

883 25. Carvalho, C. *et al.* Chromosomal G-dark bands determine the spatial organization of
884 centromeric heterochromatin in the nucleus. *Mol Biol Cell* **12**, 3563–3572 (2001).

885 26. Dillinger, S., Straub, T. & Németh, A. Nucleolus association of chromosomal domains is
886 largely maintained in cellular senescence despite massive nuclear reorganisation. *PLoS*
887 *One* **12**, e0178821 (2017).

888 27. Wang, Y. & DiMario, P. Loss of Drosophila nucleostemin 2 (NS2) blocks nucleolar release
889 of the 60S subunit leading to ribosome stress. *Chromosoma* **126**, 375–388 (2017).

890 28. Farrell, J. A. & O'Farrell, P. H. From Egg to Gastrula: How the Cell Cycle Is Remodeled
891 During the Drosophila Mid-Blastula Transition. *Annu Rev Genet* **48**, 269–294 (2014).

892 29. Falahati, H., Pelham-Webb, B., Blythe, S. & Wieschaus, E. Nucleation by rRNA dictates
893 the precision of nucleolus assembly. *Current Biology* **26**, 277–285 (2016).

894 30. Warsinger-Pepe, N., Li, D. & Yamashita, Y. M. Regulation of Nucleolar Dominance in
895 Drosophila melanogaster. *Genetics* **214**, 991–1004 (2020).

896 31. Greil, F. & Ahmad, K. Nucleolar Dominance of the Y Chromosome in Drosophila
897 melanogaster. *Genetics* **191**, 1119–1128 (2012).

898 32. Pontvianne, F. *et al.* Subnuclear partitioning of rRNA genes between the nucleolus and
899 nucleoplasm reflects alternative epiallelic states. *Genes Dev* **27**, 1545–1550 (2013).

900 33. Berry, J. *et al.* RNA transcription modulates phase transition-driven nuclear body
901 assembly. *Proc Natl Acad Sci U S A* **112**, E5237–E5245 (2015).

902 34. Lacy, M. E. & Hutson, M. S. Amnioserosa development and function in Drosophila
903 embryogenesis: Critical mechanical roles for an extraembryonic tissue. *Developmental*
904 *Dynamics* **245**, 558–568 (2016).

905 35. M'Saad, O. & Bewersdorf, J. Light microscopy of proteins in their ultrastructural context.
906 *Nature Communications 2020 11:1* **11**, 1–15 (2020).

907 36. Falahati, H. & Wieschaus, E. Independent active and thermodynamic processes govern
908 the nucleolus assembly in vivo. *Proceedings of the National Academy of Sciences* **114**,
909 1335–1340 (2017).

910 37. Torza, S. & Mason, S. G. Coalescence of Two Immiscible Liquid Drops. *Science (1979)*
911 **163**, 813–814 (1969).

912 38. Kelley, F. M., Favetta, B., Regy, R. M., Mittal, J. & Schuster, B. S. Amphiphilic proteins
913 coassemble into multiphasic condensates and act as biomolecular surfactants. *Proc Natl*
914 *Acad Sci U S A* **118**, e2109967118 (2021).

915 39. Zaffran, S. *et al.* A Drosophila RNA helicase gene, pitchoune, is required for cell growth
916 and proliferation and is a potential target of d-Myc. *Development* **125**, 3571–3584 (1998).

917 40. Thiru, A. *et al.* Structural basis of HP1/PXVXL motif peptide interactions and HP1
918 localisation to heterochromatin. *EMBO J* **23**, 489 (2004).

919 41. Smothers, J. F. & Henikoff, S. The HP1 chromo shadow domain binds a consensus
920 peptide pentamer. *Current Biology* **10**, 27–30 (2000).

921 42. Overwijn, D. & Hondele, M. DEAD-box ATPases as regulators of biomolecular
922 condensates and membrane-less organelles. *Trends Biochem Sci* **48**, 244–258 (2023).

923 43. Zhang, H. *et al.* DEAD-Box Helicase 18 Counteracts PRC2 to Safeguard Ribosomal DNA
924 in Pluripotency Regulation. *Cell Rep* **30**, 81-97.e7 (2020).

925 44. Pause, A. & Sonenberg, N. Mutational analysis of a DEAD box RNA helicase: the
926 mammalian translation initiation factor eIF-4A. *EMBO J* **11**, 2643–2654 (1992).

927 45. Hug, C. B. & Vaquerizas, J. M. The Birth of the 3D Genome during Early Embryonic
928 Development. *Trends Genet* **34**, 903–914 (2018).

929 46. Sawh, A. N. *et al.* Lamina-Dependent Stretching and Unconventional Chromosome
930 Compartments in Early C. elegans Embryos. *Mol Cell* **78**, 96-111.e6 (2020).

931 47. Aguirre-Lavin, T. *et al.* 3D-FISH analysis of embryonic nuclei in mouse highlights several
932 abrupt changes of nuclear organization during preimplantation development. *BMC Dev*
933 *Biol* **12**, 1–20 (2012).

934 48. Bizhanova, A., Yan, A., Yu, J., Zhu, L. J. & Kaufman, P. D. Distinct features of nucleolus-
935 associated domains in mouse embryonic stem cells. *Chromosoma* **129**, 121–139 (2020).

936 49. Ogienko, A. A., Korepina, M. O., Pindyurin, A. V. & Omelina, E. S. New Functional Motifs
937 for the Targeted Localization of Proteins to the Nucleolus in Drosophila and Human Cells.
938 *Int J Mol Sci* **25**, (2024).

939 50. Dembowski, J. A., Kuo, B. & Woolford, J. L. Has1 regulates consecutive maturation and
940 processing steps for assembly of 60S ribosomal subunits. *Nucleic Acids Res* **41**, 7889
941 (2013).

942 51. Boeynaems, S. *et al.* Poly(A)-binding protein is an ataxin-2 chaperone that regulates
943 biomolecular condensates. *Mol Cell* **83**, 2020-2034.e6 (2023).

944 52. Padeken, J. *et al.* The Nucleoplasmin Homolog NLP Mediates Centromere Clustering
945 and Anchoring to the Nucleolus. *Mol Cell* **50**, 236–249 (2013).

946 53. Holmberg Olausson, K., Nistér, M. & Lindström, M. S. Loss of nucleolar histone
947 chaperone NPM1 triggers rearrangement of heterochromatin and synergizes with a
948 deficiency in DNA methyltransferase DNMT3A to drive ribosomal DNA transcription.
949 *Journal of Biological Chemistry* **289**, 34601–34619 (2014).

950 54. Sanchez-Burgos, I., Joseph, J. A., Collepardo-Guevara, R. & Espinosa, J. R. Size
951 conservation emerges spontaneously in biomolecular condensates formed by scaffolds
952 and surfactant clients. *Scientific Reports 2021 11:1* **11**, 1–10 (2021).

953 55. Schmit, J. D., Feric, M. & Dundr, M. How Hierarchical Interactions Make Membraneless
954 Organelles Tick Like Clockwork. *Trends Biochem Sci* **46**, 525–534 (2021).

955 56. Alberti, S. & Hyman, A. A. Biomolecular condensates at the nexus of cellular stress,
956 protein aggregation disease and ageing. *Nature Reviews Molecular Cell Biology 2021*
957 *22:3* **22**, 196–213 (2021).

958 57. Wachsmuth, M., Knoch, T. A. & Rippe, K. Dynamic properties of independent chromatin
959 domains measured by correlation spectroscopy in living cells. *Epigenetics Chromatin* **9**,
960 1–20 (2016).

961 58. Thompson, A. P. *et al.* LAMMPS - a flexible simulation tool for particle-based materials
962 modeling at the atomic, meso, and continuum scales. *Comput Phys Commun* **271**,
963 108171 (2022).

964 59. Bajpai, G. & Safran, S. Mesoscale, long-time mixing of chromosomes and its connection
965 to polymer dynamics. *PLoS Comput Biol* **19**, e1011142 (2023).

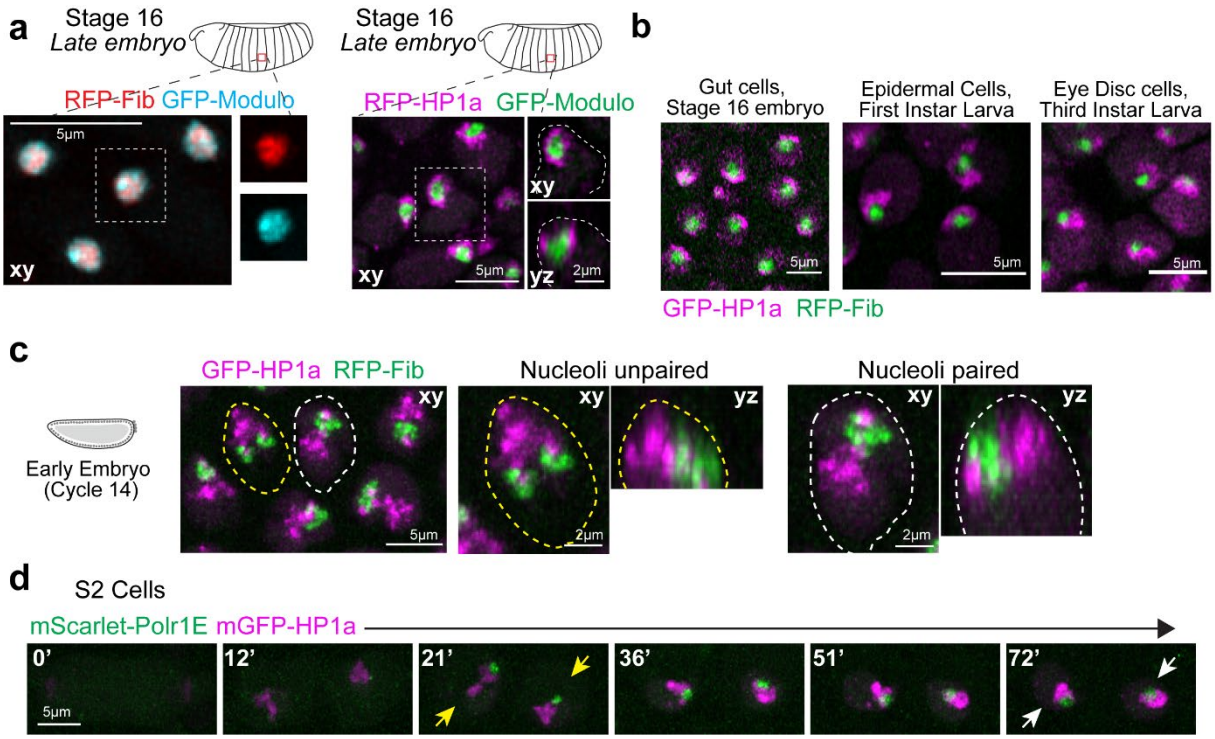

Extended Data Fig. 1: PCH organization relative to the nucleolus in Drosophila embryos, larval tissues, and cultures cell lines. (**a**) (Left) Distribution of GFP-Modulo (cyan) and RFP-Fibrillarin (red) in nucleoli of a live late-stage (Stage 16) embryo. (Right) Maximum intensity projections showing PCH localization labeled with RFP-HP1a (magenta) and nucleoli marked by GFP-Modulo (green) in live epidermal nuclei from a late-stage *Drosophila* embryo (Stage 16, ~14-16hr). The nucleus outlined by the white dashed box is magnified and presented in xy and xz views, with white dashed lines indicating the nuclear boundary. (**b**) Stills of live nuclei expressing GFP-HP1a (magenta) and RFP-Fib (green) in gut cells from a Stage 16 embryo, first instar larval epidermal cells, and third instar larval eye disc. (**c**) Nuclei from Cycle 14 embryos expressing GFP-HP1a (magenta) and RFP-Fib (green), showing two unpaired nucleoli (yellow dashed line) and one paired nucleolus (white dashed line). Both nuclei have been enlarged to show the "extended" conformation of HP1a relative to the nucleolus in the xy and yz views. (**d**) Time-lapse stills of two daughter S2 cells exiting mitosis, transfected with mScarlet-Polr1E, a Pol-I subunit (green) and mGFP-HP1a (magenta). Numbers on the top left corner indicate time in minutes from the end of mitosis. Yellow arrows indicate HP1a in an extended conformation from the nucleolus, while white arrows indicate HP1a in the surrounded conformation.

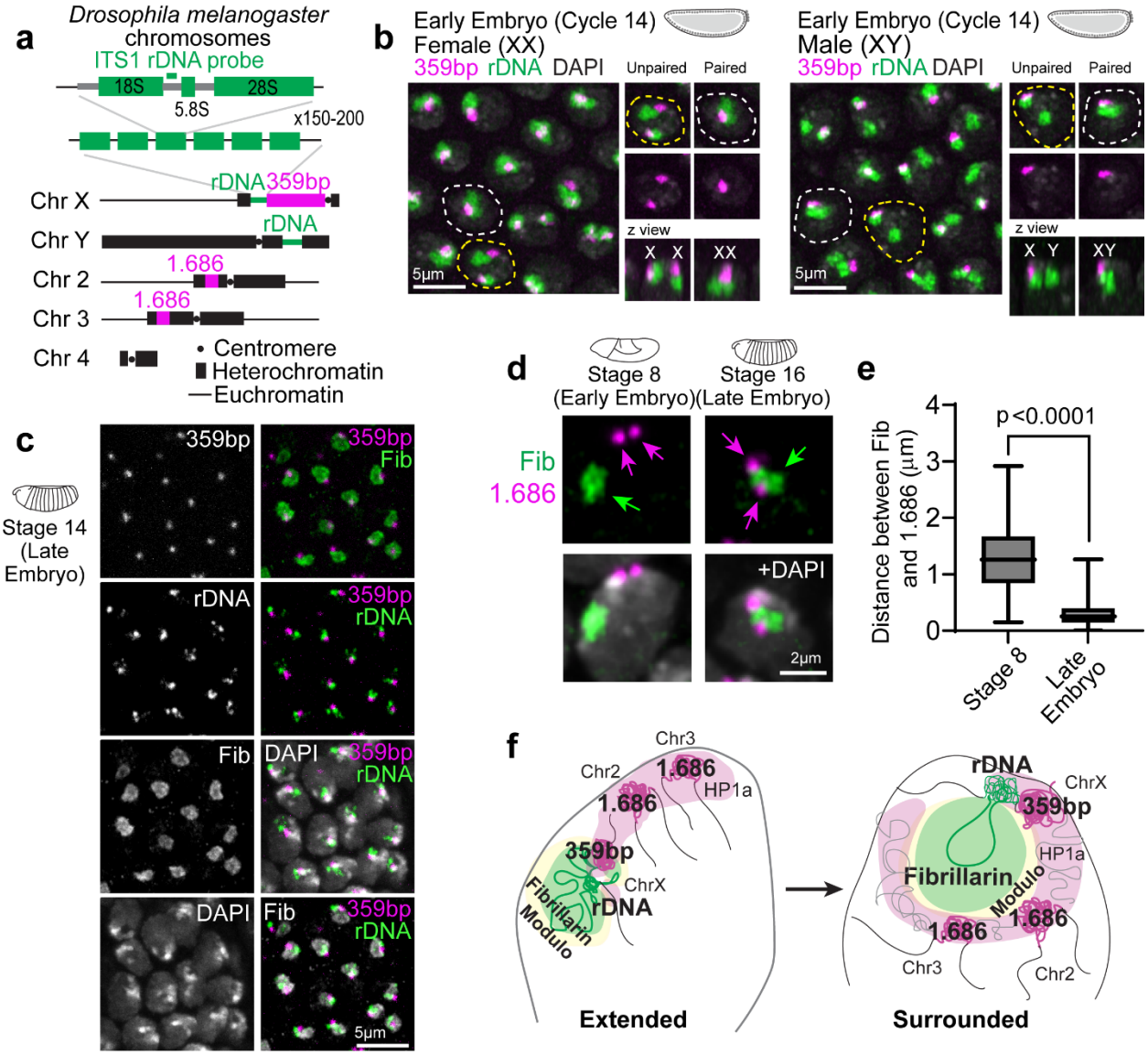

Extended Data Fig. 2: Dynamics of PCH reorganization relative to the nucleolus during *Drosophila* embryonic development. (**a**) Schematic representation of pericentromeric satellite repeats (359bp and 1.686) and rDNA repeats in *Drosophila* melanogaster chromosomes. The schematic of ribosomal DNA (rDNA) arrays indicates the position of the ITS-1 rDNA probe used for FISH. (**b**) Localization of 359bp satellite DNA (magenta) and rDNA (green) in female and male early (Cycle 14) embryos. The dashed white line indicates a nucleus with paired nucleoli, while the dashed yellow line marks a nucleus with unpaired nucleoli. The nuclear boundary is determined by DAPI staining. (**c**) Combined immuno-FISH stained for 359bp, ITS-1 rDNA, Fibrillarin, and DAPI in late embryos. (**d**) Combined immuno-FISH of 1.686 (magenta arrows), Fibrillarin (green arrow) and DAPI (grey) in a nucleus from epidermal cells of early (Stage 8, ~Cycle 15) and late (Stage 16) *Drosophila* embryos. (**e**) Distance between the centers of geometry of 1.686 and Fibrillarin in Stage 8 (~Cycle 15) and Stage 16 (Late) in *Drosophila* nuclei. n>60 loci (from 3 embryos) at each developmental stage. Bar graphs extend from 25th to 75th percentile, error bars: min to max. (**f**) Schematic summarizing the dynamic reorganization of nucleoli and PCH during *Drosophila* development, highlighting key proteins and DNA elements involved.

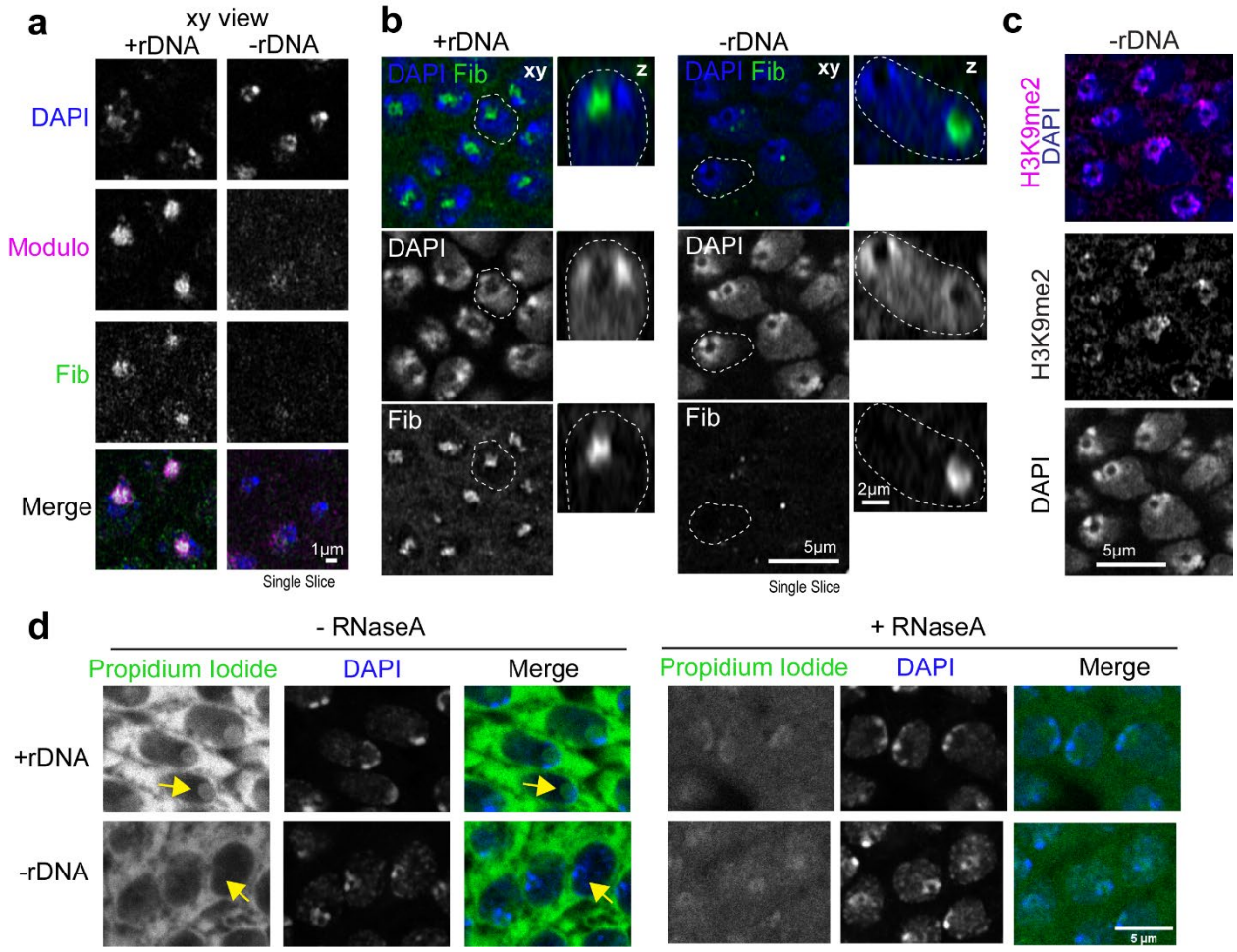

Extended Data Fig. 3: The PCH void in -rDNA embryos does not stain for DAPI, Fibrillarin, Modulo, H3K9me2 or Propidium Iodide (RNA). (**a**) Representative images of fixed nuclei from wildtype late embryos and mutant embryos lacking rDNA stained for Modulo (magenta), Fibrillarin (green) and DAPI (blue). (**b**) Left: Representative images of fixed nuclei from Stage 14-16 (late) wildtype embryos and mutant embryos lacking rDNA showing Fibrillarin (green) and DAPI (blue). Right: Nuclei marked with white dashed outlines on the left are shown in the z plane. (**c**) H3K9me2 immunofluorescence (magenta) and DAPI (blue) staining in -rDNA nuclei in Stage 14-16 (late) *Drosophila* embryos. (**d**) Representative images of fixed nuclei from Stage 14-16 (late) wildtype and mutant embryos lacking rDNA stained with Propidium Iodide (green) and DAPI (blue) without (left) and with (right) RNaseA. The yellow arrow points to the RNA staining in the nucleolus in +rDNA and lack of propodium iodide staining in the PCH void of -rDNA nuclei.

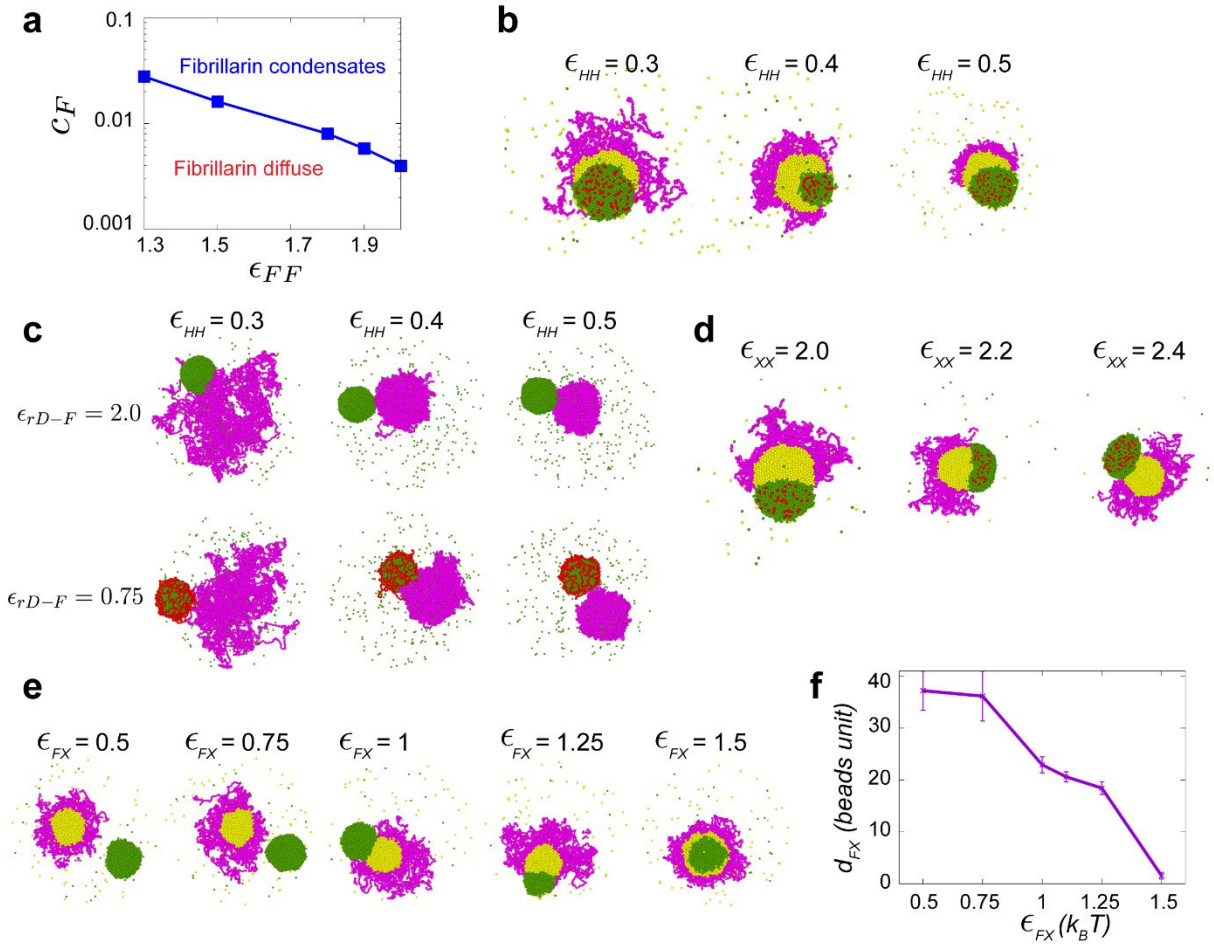

Extended Data Fig. 4: Coarse-grained model for the assembly of the nucleolus and PCH. (**a**) The phase diagram illustrates the minimum attraction strength required to condense Fibrillarin at different concentrations. (**b**) Simulation endpoint snapshots depict the outcomes of varying the attraction strengths between beads of the PCH (H) polymer chain (ϵ_{HH}). (**c**) Simulation snapshots depict varying attraction strengths between rDNA-Fibrillarin (top to bottom) and beads of the PCH polymer chain (left to right). (**d**) Simulation endpoint snapshots depict the outcomes of varying X-X attraction strengths (ϵ_{XX}). (**e**) Simulation endpoint snapshots depict the outcomes of varying attraction strengths between Fibrillarin and protein X (ϵ_{FX}) in the -rDNA condition. (**f**) The average distance (d_{FX}) between Fibrillarin and protein X condensates from their center of mass is measured for different attraction strengths. Error Bars represent s.d.

a

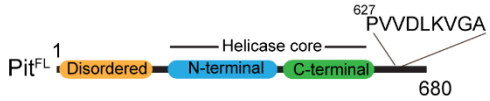


```
Alignment within Drosophila:

D. melanogaster Pit          IFNVNTLDLQAVAKSFGFLVPPVVDLKVGAAKRERPEKRVGGGGFGFYKKMNE-GSASKQ
D. simulans                  IFNVNTLDLQAVAKSFGFLVPPVVDLKVGAAKRERPEKRVGGGGFGFYKKMNE-GSASKQ
D. sechellia                 IFNVNTLDLQAVAKSFGFLVPPVVDLKVGAAKRERPEKRVGGGGFGFYKKMNE-GSASKQ
D. yakuba                    IFNVNTLDLQAVAKSFGFLVPPVVDLKVGAAKRERPEKRVGGGGFGFYKKMNE-GSASKQ
D. erecta                    IFNVNTLDLQAVAKSFGFLVPPVVDLKVGAAKRERPEKRVGGGGFGFYKKMNE-GSASKQ
D. virilis                   IFNVNTLDLQAVSKSFGFLVPPVVDLKVGAAKRERPEKRVGGGGFGYYKQMNDSGA--KQ
D. mojavensis                IFNVNTLDLQAVAKSFGFLVPPVVDLKVGAAKRERPEKRVGGGGFGYYKQMNERGGGHKQ
D. persimilis                IFNVNTLDLQAVSKSFGFLVPPVVDLKVGAAKRQRPEKRVGGGGFGYYRQMND-TSASKQ
D. pseudoobscura             IFNVNTLDLQAVSKSFGFLVPPVVDLKVGAAKRQRPEKRVGGGGFGYYRQMND-TSASKQ
D. ananassae                 IFNVNTLDLQAVAKSFGFLVPPVVDLKVGAAKRERPEKRVGGGGFGYYKKMNE-GSDSKQ
D. grimshawi                 IFNVNTLDLQAVSKSFGFLVPPVVDLKVGAAKRERPEKRVGGGGFGYYKQMNDNSS--KQ
D. willistoni                IFNVNTLDLQAVAKSFGFLVPPVVDLKVGAAKRQRPEKRMGGGGFGYYKQMND---TNKQ
                             ************ ******************** ***** ****** *  **      **
Alignment across species:

D. melanogaster Pit           QIFNVNTLDLQAVAKSFGFLVPPVVDLK--VGAA-KRERPEKRVGGGGFGFYKKMNE
D. rerio ddx18                QIYNVETLDLPKVAMSFGFKVPPFVDLN--VHSS-KGVKLHKRGGGGGFGYQKSKN-
H. sapiens DDX18              QIFNVNNLNLPQVALSFGFKVPPFVDLN--VNSN-EG-KQKKRGGGGGFGYQKTKK-
M. musculus Ddx18             QIFNVNNLNLPQVALSFGFKVPPFVDLN--VSSH-DG-KLKKRGGGGGFGYQKTKK-
C. elegans B0511.6            DIFDVTNMDLTAVSKSFGFSVPPFVDLP--ISNK-PKVEIRSKLSGAGYRKKKQSFT
S. pombe has1                 SIFDINKLDLAKVAKSFGFAHPPNVNIT--IGAS-GR--TDKKERRAGYNKKNHVDV
S. cerevisiae HAS1            TVYQIDKLDLAKVAKSYGFPVPPKVNIT--IGAS-GK--TPNTKRR-----KTHK--
A. thaliana AT3G18600         EIFDVSKLSIENFSASLGLPMTPRIRFT..VGAEMRKADIEDKKVDKERRREKRMKQ
                                                   * *    *
```

Extended Data Fig. 5: Pitchoune has a conserved PxVxL HP1a-interacting motif. (**a**) Evolutionary analysis to determine the conserved PxVxL motif in Pitchoune within *Drosophila* species (top) and across non-*Drosophila* eukaryotic model organisms (bottom).

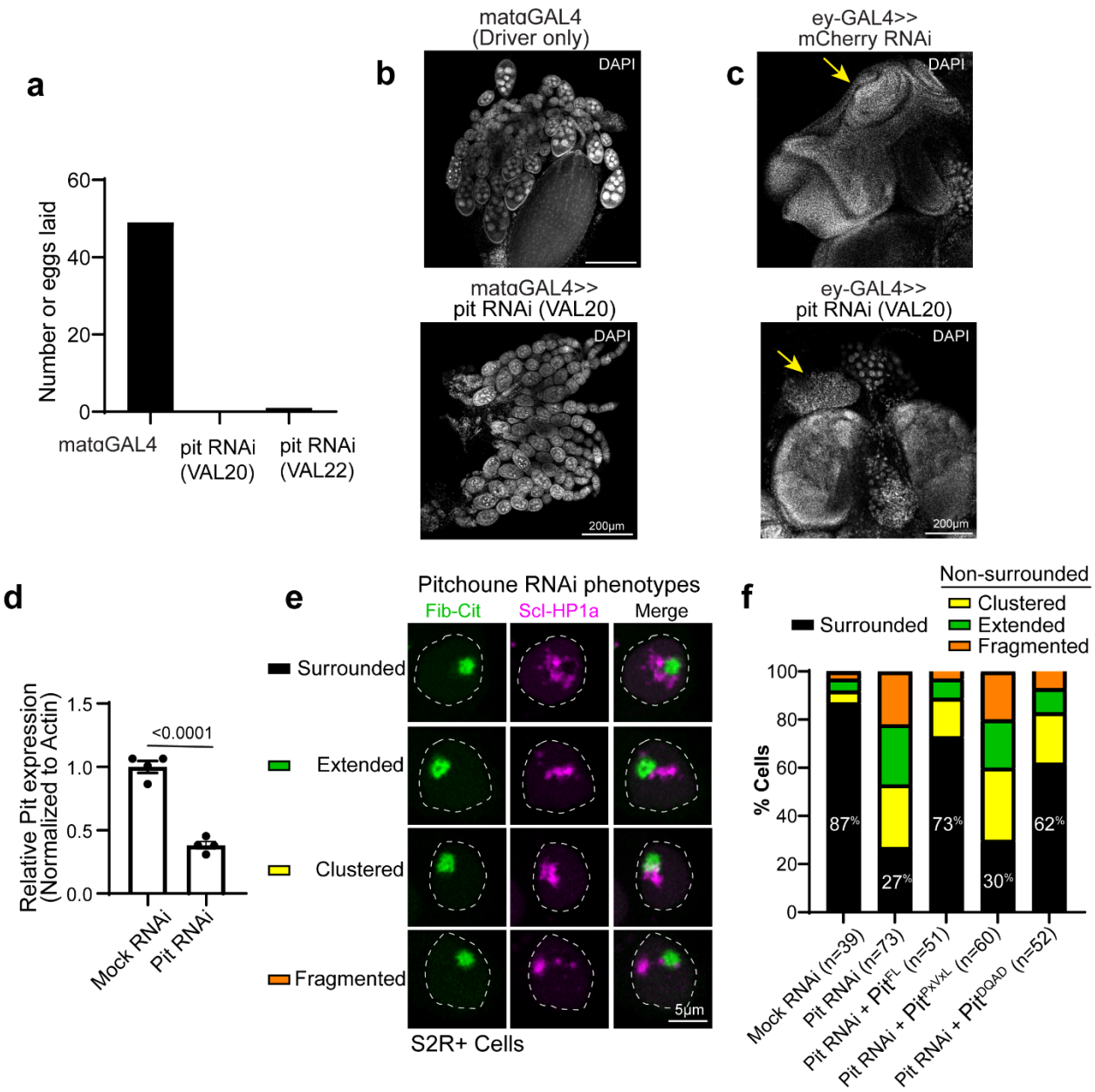

Extended Data Fig. 6: Developmental defects and HP1a disorganization phenotypes due to Pitchoune knockdown in Drosophila tissues and cultured cells. (**a**) Number of eggs laid on an apple juice plate after a 3hr collection in mataGAL4 (driver only) and mataGAL4 driving UAS-Pitchoune RNAi (VAL20 and VAL22 lines). (**b**) Representative images of dissected ovaries in control (mataGAL4, driver only) and after Pitchoune knockdown stained with DAPI. (**c**) Representative images of dissected eye antennal discs (yellow arrow) in control (ey-GAL4>mCherry RNAi) and after Pitchoune knockdown (ey-GAL4>pit RNAi, VAL20) stained with DAPI. (**d**) Quantitation of Pitchoune transcripts using qPCR to confirm the knock-down of Pitchoune, normalized to actin. Bar graphs depict mean ± s.e.m. n=4 biological replicates. (**e**) Representative nuclei transfected with Fib-Citrine and Scarlet-I-HP1a, showing four categories of HP1a distribution phenotypes observed after Pitchoune knockdown. (**f**) Quantification of the % nuclei with Surrounded, Extended, Clustered, and Fragmented HP1a phenotype after Pitchoune RNAi and its rescue with Pit^{FL}, Pit^{PxVxL}, and Pit^{DQVD}.

LEGENDS FOR SUPPLEMENTARY MOVIES

966 **Supplementary Movie 1:** 3D rendering of RFP-Fib (green) and GFP-HP1a (magenta) in
967 epidermal cells of a Stage 16 Drosophila embryo.

968 **Supplementary Movie 2:** Live imaging of RFP-Fib (green) and GFP-HP1a (magenta) in nuclear
969 cycle 13 of Drosophila embryogenesis.

970 **Supplementary Movie 3:** Live imaging of RFP-Fib (green) and GFP-HP1a (magenta) in nuclear
971 cycle 14 of Drosophila embryogenesis.

972 **Supplementary Movie 4:** Live imaging of RFP-Fib (green) and GFP-HP1a (magenta) in nuclear
973 cycle 15 of Drosophila embryogenesis.

974 **Supplementary Movie 5:** Live imaging of RFP-Fib (green) and GFP-HP1a (magenta) in nuclear
975 cycle 16 of Drosophila embryogenesis.

976 **Supplementary Movie 6:** Live imaging of RFP-Fib (green) and GFP-HP1a (magenta) in nuclear
977 cycle 17 of Drosophila embryogenesis.

978 **Supplementary Movie 7:** Live imaging of GFP-Fib (green) and RFP-HP1a (magenta) in nuclear
979 amnioserosa nuclei in embryos lacking rDNA.

980 **Supplementary Movie 8:** Simulations of coarse-grained modeling of rDNA (red), Fibrillarin
981 (green), PCH (magenta), and an amphiphilic protein (yellow) with the parameters listed in the 4X4
982 matrix in Fig. 4c.

983 **Supplementary Movie 9:** Live imaging of Pitchoune-GFP (green) and RFP-HP1a (magenta) in
984 nuclear amnioserosa nuclei in embryos lacking rDNA.